Microphysical evolution and column loading drive nonlinear regional contrast in black carbon top-of-atmosphere forcing

Pravash Tiwari[1], Jason Blake Cohen[1], Hongrui Gao[1], Lingxiao Lu[1], Jun Wang[2], Oleg Dubovik[3], Kai Qin[1]

[1]School of Environment and Spatial Informatics, China University of Mining and Technology, Xuzhou 221116, China
[2]Department of Chemical and Biochemical Engineering, University of Iowa, Iowa City, IA, USA
[3]University of Lille, CNRS, UMR 8518 – LOA – Laboratoire d'Optique Atmosphérique, 59000 Lille, France

Correspondence to: Jason Blake Cohen (jasonbc@alum.mit.edu ; jasonbc@cumt.edu.cn)

Abstract. Black carbon (BC) aerosols remain among the most uncertain contributors to anthropogenic climate forcing, as their radiative impact depends sensitively on microphysical evolution and atmospheric loading. This study presents a physics-informed, machine learning (ML) approach to estimate clear-sky BC top-of-atmosphere direct radiative forcing (BCTOA) at high spatial-temporal resolution while retaining physical interpretability. The study derives necessary optical properties for radiative transfer modeling (RTM), by constraining them with multi-platform, multi-waveband observations and their associated uncertainties. The RTM outputs are then used to train the ML surrogates and applied over two contrasting urban agglomerates-Xuzhou, China, and Dhaka, Bangladesh. The ML framework closely reproduces physics-based regional climatological mean (-17.6 ± 2.2 W m^{-2} versus -17.4 ± 2.6 W m^{-2} over Xuzhou; -14.9 ± 1.1 W m^{-2} versus -15.0 ± 1.2 W m^{-2} for Dhaka), while achieving high predictive fidelity $R^2 > 0.95$; RMSE ~1.5–1.8 W m^{-2} and strong cross-regional consistency (r > 0.9). Predictor decomposition reveals BCTOA is primarily modulated by BC aerosol optical depth (BCAOD), column number density, and mixing state, with their relative importance and influence varying non-linearly across cooling-to-warming regimes. Crucially, similar BC loading can yield contrasting absorption-scattering dynamics across region, which are not captured by simplfied forcing parameterization. Together, the physics-informed ML framework and the multi-domain evaluation provide an efficient and transferable tool for constraining BC radiative impacts across real-world heterogeneity. The analysis also offers new mechanistic insight into how regional properties reshape BC regional radiative forcing.

1 Introduction

Among the major climate forcers, aerosols represent one of the largest sources of uncertainty in Earth's radiative budget, primarily through their interactions with solar and terrestrial radiation. These radiative perturbations arise through key aerosol-radiation interactions and manifest as the direct aerosol effect (Chung, 2012; Yu et al., 2006); the indirect aerosol effect (Lohmann and Feichter, 2005; Nenes et al., 2002) and the semi-direct effect (Koch and Del Genio, 2010; Randles and Ramaswamy, 2010). Despite an estimated net global cooling of around -1.3 ± 0.7 W m^{-2} from anthropogenic aerosols−offsetting ~33% of the GHGs warming (Li et al., 2022), their radiative forcing quantification remains highly uncertain and poorly constrained. The diverse optical and microphysical characteristics of aerosol species (Li et al., 2022), adds to the substantial spread in aerosol's direct radiative forcing (DRF), amplifying uncertainties in climate sensitivity.

Black carbon (BC) aerosols, emitted primarily from incomplete combustion of carbon exerts strong solar-radiation integrated absorption, impacting regional radiative forcing and heating, where it locally competes with greenhouse gases like CO_2 and CH_4 (Hansen and Sato, 2001; Jacobson, 2001). Yet, it's DRF estimates vary widely, for instance, one study reported a global BC instantaneous radiative forcing of +0.9 W m^{-2} (+0.4 to +1.2 W m^{-2}) (Ramanathan and Carmichael, 2008). In contrast, AeroCom Phase II yielded a lower estimate of +0.23 W m^{-2} (Myhre et al., 2013). AERONET-derived absorption aerosol optical depth (AAOD) analyses suggested +0.51 W m^{-2} (+0.06 to +0.91 W m^{-2}) (Bond et al., 2013), while the IPCC AR5 synthesized expert judgment estimating +0.4 W m^{-2} (+0.05 to +0.8 W m^{-2}) (Bond et al., 2013; Myhre et al., 2013). The recent IPCC AR6 reports a ~50% reduction in BC warming and an associated top of the atmospheric (TOA) increase by 0.1° (Forster et al., 2023) due to adjusted rapid climate responses (Everett et al., 2022), however, several studies emphasize that emission products used by the CMIP-6 models (used in the IPCC AR6) didn't adequately account for BC loading as well as varying absorption incurred from dynamic variability in morphological complexities (Chen et al., 2022; Kelesidis et al., 2022; Ramachandran et al., 2023).

Both ground and satellite-based observational communities are rigorously working to improve quantification of BCDRF regionally. Ground-based BC mass measurements and/or sun–sky photometer's aerosol optical depth (AOD) provide some essential constraints for optical modeling. These are typically used in iterative Mie model frameworks to derive single scatter albedo (SSA), phase function and asymmetry coefficient (ASY) for radiative transfer model (RTM) simulations(Mehrotra et al., 2024; Zeb et al., 2020). However, these approaches are spatially limited, rely on limited size bins and lacks ability to resolve internal mixing. Furthermore, few observational studies have either interpolated or extrapolated absorption or extinction between a small number of distinct wavebands (where observations are taken) and/or use fixed mass absorption coefficients (MAC of 7.5 ± 1.2 m^2/g and 8.0 ± 0.7 m^2/g at 550nm) (Liu et al., 2020a; Randles et al., 2017; Zangmeister et al., 2018) to compute BC DRF. Satellite-based approaches extend the spatial coverage to better capture regional variability of regional aerosol DRF (Bellouin et al., 2005; Kahn et al., 2023; Matus et al., 2019; Wu et al., 2024). The Clouds and the Earth's Radiant Energy System (CERES) and CloudSat (2B-FLXHR-LIDAR) provides a comprehensive dataset of TOA fluxes which are widely used (Gautam et al., 2023; Loeb et al., 2021; Subba et al., 2020, 2022). While these approaches have analyzed total

65   aerosol DRF, however, accurate isolation of BC signals from co-existing aerosol types within the satellite data is challenging. Furthermore, computing no-aerosol fluxes to derive the net TOA forcing adds to the existing challenge. Studies often assume either linear AOD–flux relationships (computing TOA$_{\text{no-aerosol-flux}}$ at AOD =0) or using low-aerosol pixels for pristine flux. However, such approaches can introduce significant uncertainties in regions undergoing rapid industrialization or experiencing persistently high aerosol loading. such as South and East Asia, where truly pristine conditions are rare and the aerosol–radiation

70   interactions are highly nonlinear. Finally, many satellite derived DRF approaches rely on single-wavelength absorption measurements (commonly at 500 or 550 nm), which increases DRF uncertainty as it neglects the spectral dependence of aerosol–radiation interactions across the solar spectrum. Complementarily, reanalysis products like MERRA-2 and CAMS assimilate multi-source data and provide different BC specific properties. However, these products also also incorporate simplified aerosol representations like using pre-defined morphology with median radii and standard deviations that are

75   climatologically fixed limiting reanalysis accuracy (Chen et al., 2023; Chin et al., 2002; Ding and Liu, 2022). Moreover, emissions datasets underlaying these assimilations are often outdated (Li et al., 2024), particularly over many rapidly developing and industrial areas in the Global South (Dasari et al., 2020; Ren et al., 2025), and many employ externally mixed tracers (Fernandes et al., 2023; Xu et al., 2020) rather than internal mixtures.

       Overall, these approaches have advanced our understanding of aerosol DRF, but still leave persistent gaps in capturing BC's

80   dynamic radiative behavior at regional scales. The underlaying uncertainties in BC DRF quantifications are further aggravated at regional level, due to BC's short atmospheric lifetime, rapidly evolving microphysics and multispectral absorption interaction. Reducing these discrepancies requires a geospatially resolved approach that uses multi-waveband information, considers both columnar loading and per-particle properties in tandem (Tiwari et al., 2023). Additionally, an improved accounting of emissions also requires accurate knowledge of microphysical evolution (Fierce et al., 2020; Liu et al., 2017),

85   morphological dynamics (Wu et al., 2018), and vertical lofting of BC (Cohen and Wang, 2014). Accurate regional BC DRF quantification is therefore critical, not only to resolve local radiative impacts but also to reduce uncertainties in global forcing estimates.

       In light of persistent challenges in regional BCDRF quantification and building on recent advances in observationally constrained BC microphysical retrievals, including the core-shell Mie model optimization (COSMO), this study extends and

90   refines multi-platform framework of an earlier approach developed by Tiwari et al., (2025). That framework combined multi-wavelength observations with a flexible core–shell morphology to derive probabilistic BC microphysical solutions and column densities, jointly constrained by multi-band SSA. Here, we introduce an additional observational constraint through multi-satellite total AOD inputs, further optimizing the estimation of BC size, mixing state, and column loading, along with their associated optical properties. These physically consistent ensembles are then coupled with RTM to generate high resolution

95   BCTOA DRF. Finally, we train a set of linear, parametric and interpretable machine learning (ML) surrogate models on these COSMO-RTM outputs to test their predictive skills, provide a fast and transferable tool for estimating BC TOA DRF and diagnosing how BC microphysics modulate radiative forcing. Unlike most previous assessments which have generally not incorporated dynamically varying size–mixing states (e.g. Luo et al., 2022; Romshoo et al., 2024; Yang et al., 2025) or jointly

constrained microphysics and column loading in TOA forcing calculations (e.g. Tiwari et al., 2023), this unified approach
100   integrates these aspects to enhance understanding of regional BC radiative forcing while providing a physically interpretable,
transferable and computationally efficient modeling tool and explore new aspects of BC's microphysical and column property
influence on clear-sky instantaneous BCTOA .

2 Methodology

2.1 Computing BC TOA DRF from observationally constrained microphysics and RTM

105   Tiwari et al., (2025) used a multi-platform COSMO approach to derive BC aerosol size, mixing state, and column densities
over Xuzhou, China and greater Dhaka, Bangladesh. Greater Dhaka is one urban agglomeration representing a rapidly
expanding monocentric megacity in a tropical river delta along with its per-urban settlements. They are characterized by intense
emissions from traffic, brick kilns, and small-scale industries along the inland river networks. In contrast, Xuzhou, as the
largest city in the Huaihai region is a polycentric urban agglomeration on the North China Plain, where it acts as a central node
110   in a network of cities with significant heavy industry, energy production, and agriculture. Comparing these two regions
provides unique insights into how different urban forms and regional economic structures influence the physical and optical
properties of light-absorbing aerosols.

The original framework combined multi-waveband single-scattering albedo (SSA) from TROPOMI (388 nm) and
AERONET/SONET (440-1020 nm) observations for these regions and used a two-component Mie inversion to generate
115   ensembles of physically consistent microphysical solutions for BC core and non-absorbing shell sizes while accounting for
both waveband offsets and cross-platform SSA uncertainties at a grid-by-grid and day-by-day level. A brief description of the
Mie model framework and assumed morphological set up, including key assumptions and their rationale, is provided in
Appendix A. In essence, Tiwari et al., (2025) first constructed multi-waveband SSA ranges at each grid based on their
uncertainties and waveband offsets. Since each BC particle interacts with radiation across all wavebands simultaneously, the
120   COSMO was used to generate paired core-shell size solutions that are physically consistent across the spectrum. Each
candidate size pair was evaluated by comparing its modeled SSA at multiple wavebands to the uncertainty-bounded SSA
ranges. Only those solutions with SSA values falling within the SSA uncertainty range at all wavebands simultaneously were
retained. This filtering approaches been previously implemented using both ground and satellite SSA observations, both in
tandem as well as separately (Liu et al., 2024b, a, c; Wang et al., 2021) . The multi-waveband SSA constraining ensures that
125   the resulting microphysical ensembles reflect only BC core/sulfate shell pairs capable of reproducing the observed, uncertainty-
aware SSA constraints across the full spectral domain. For more details on the geographical context of the urban agglomerates
including, differences in emission characteristics of Xuzhou and greater Dhaka region, and the application of the multi-
platform COSMO with SSA constraint to derive BC microphysics and derivation of BC column loading, readers are referred
to Tiwari et al., (2025).

130   This study extends and refines the framework, where it uses the probabilistic solutions of core and shell sizes and total column mass density derived from earlier SSA constraint for computing BC aerosol optical depth (BCAOD) across multiple wavelengths. The BCAOD calculation follows a forward Mie-based physical formulation. Specifically, the diameters of the BC core (D_{core}) and total diameter (D) of the particle are used to determine the particle's geometric cross-sectional area (σ_g), which reflects the amount of light that the particles interact with. Next, the volumes of the BC core (V_{core}), SUL shell (V_{shell}),

135   and total particle volume (V_{total}) are used to establish the effective density of the aerosol ρ_{total} based on the volume weighted of BC (ρ_{BC}) and sulfate (ρ_{SUL}). Subsequently, the mass of a single particle (m_p) is calculated by multiplying its total volume (V_{total}) by its effective density (ρ_{total}). The mass extinction efficiency (α_{ext}) is then computed to assess how effectively the particle contributes to light extinction per unit mass using extinction efficiency (Q_{ext}). Finally, we derive the modeled BCAOD (τ_{BC}) by multiplying the mass extinction efficiency by the total aerosol mass (M_c) in the column. The mathematical formulation

140   of BCAOD computation is summarized in Eq. (1) through Eq. (8).

$$\sigma_g = \frac{\pi D^2}{4} \qquad \text{Eq 1.}$$

$$V_{core} = \frac{4}{3} \times \pi \left(\frac{D_{core}}{2}\right)^3 \qquad \text{Eq 2.}$$

$$V_{total} = \frac{4}{3} \times \pi \left(\frac{D}{2}\right)^3 \qquad \text{Eq 3.}$$

$$V_{shell} = V_{total} - V_{core} \qquad \text{Eq 4.}$$

145

$$\rho_{total} = \frac{(\rho_{BC} \times V_{core} + \rho_{SUL} \times V_{shell})}{V_{total}} \qquad \text{Eq.5}$$

$$m_p = V_{total} \times \rho_{total} \qquad \text{Eq 6.}$$

$$\alpha_{ext} = \frac{Q_{ext} \times \sigma_g}{m_p} \qquad \text{Eq 7.}$$

$$\tau_{BC} = M_c \times \alpha_{ext} \qquad \text{Eq 8.}$$

The SSA-based constraint ensures internal spectral consistency, but it does not by itself rule out microphysical solutions that

150   generate unrealistically strong BC extinction. To address this limitation, we introduce a physically binding requirement that the modeled τ_{BC} must always be less than total AOD measured in the column. Since total AOD represents the combined extinction from all aerosol species, not only BC, any case where τ_{BC} exceeds the total AOD indicates a violation and is therefore physically unrealistic. This requirement acts as an additional layer of observational constraint to refine microphysical and column loading solutions.

155   The Mie model outputs, τ_{BC}, SSA and ASY, which are computed at three wavebands 388 nm, 470 nm, and 550 nm. To implement this total AOD constraint, we derive specific upper uncertainty bounds based on AOD measurements from Multi-Angle Implementation of Atmospheric Correction (MAIAC) algorithm-based AOD (470 nm, 550 nm) (Lyapustin et al., 2018; Martins et al., 2017) and TROPOMI (388 nm). The upper limits for AOD are defined in Eq 9. to Eq 11. based on Lyapustin and Wang, (2022) and de Graaf, (2022):

160    $$\text{Upper AOD}_{388} = \text{AOD}_{388} + \max(0.1, 0.25 \times \text{AOD}_{388}) \qquad \text{Eq 9.}$$

$$\text{Upper AOD}_{470} = \text{AOD}_{470} + 0.05 + (0.1 \times \text{AOD}_{470}) \qquad \text{Eq 10.}$$

$$\text{Upper AOD}_{550} = \text{AOD}_{550} + 0.05 + (0.1 \times \text{AOD}_{550}) \qquad \text{Eq 11.}$$

We then implement the above violation condition whereby τ_{BC} must remain below the upper-bound total AOD observed across all wavebands simultaneously. If τ_{BC} exceeds the total AOD for even one waveband, that dataset is excluded from further analysis. After implementing this quality control, a total of 178 and 314 days of data were used for analysis for Xuzhou and greater Dhaka respectively from the period of 2018-04-30 to 2022-04-30, consisting of a total of 105569 and 273225 individual grid points in space and time.

The τ_{BC}, SSA and ASY at multiple wavebands, are used to within the RTM model to generate BC DRF. Additional necessary datasets, including MODIS Level 2 precipitable water vapor (PWV) (MYD05/MOD05), surface spectral albedo from the MODIS Bidirectional Reflectance Distribution Function product (MCD43A1), and total column ozone from the TROPOMI S5P_L2__O3_TOT_HiR product, were processed and spatio-temporally harmonized to align with the BC data grid resolution. The RTM model used herein, is the Santa Barbara DISORT Atmospheric Radiative Transfer (SBDART) (Ricchiazzi et al., 1998) model which generates the TOA and surface radiative forcing. The description and processing of each ancillary dataset is provided in Appendix B and mathematical formulation for calculating TOA DRF from SBDART derived fluxes are provided in Supplement section S1. A schematic overview of the workflow, encompassing BCAOD computation, multi-waveband satellite data filtering, and radiative transfer modeling, is provided in Figure 1.
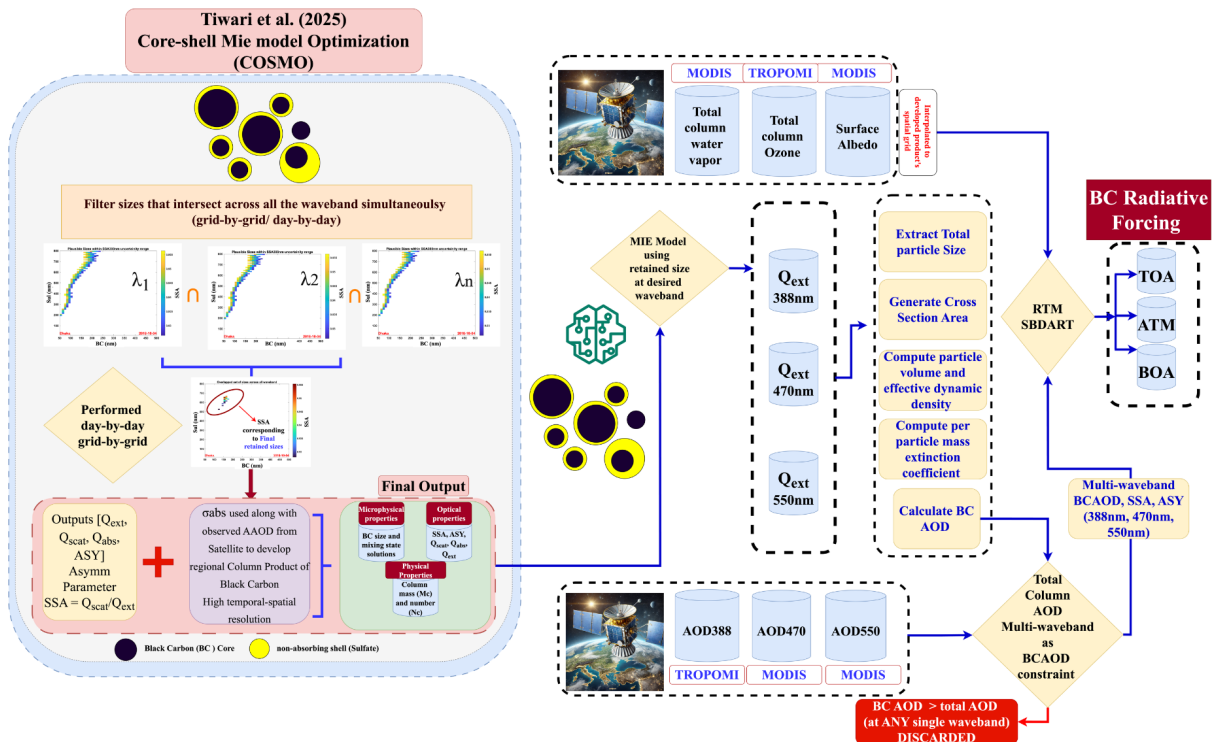

Figure 1: Overview of the COSMO-coupled RTM framework for deriving BC radiative forcing.

Overall approach integrates TROPOMI and AERONET/SONET SSAs using waveband offset adjustment and further employs observationally constrained multi-waveband inverse-forward MIE modeling to generate size, mixing state and associated optical and physical properties as detailed in Tiwari et al., (2025). This study further refines the established approach using an additional layer of observational constraint from multi-waveband aerosol optical depth. The resulting set of microphysical and associated optical properties are integrated with PWV, surface spectral albedo, and total column ozone are used to perform SBDART RTM runs and BC radiative forcing at a day-by-day and grid-by-grid resolution over Xuzhou and greater Dhaka are derived.

2.2 Surrogate Models for Rapid BCTOA DRF Estimation

High-fidelity RTMs such as SBDART, when simulated with morphologically dynamic BC aerosol properties and environmental variables can enhance the accuracy of BC DRF estimates. However, computational demands render the approach impractical for large-scale chemical transport or climate modeling applications. As a means of coping with the computational issue, the atmospheric science community often adopts a linear radiative efficiency approach specifically for total aerosol DRF, by assuming the TOA as a linear function of AOD (García et al., 2012; Sena et al., 2013; Sundström et al., 2015). While this method enables rapid regional-to-global scaling of DRF estimates using satellite AOD products, it overlooks non-linear modulations in TOA forcing caused by microphysical variability (e.g., particle size, mixing state), column number loading, and their role in both absorption and extinction efficiency.

This study explores this gap by developing three surrogate models for fast BC radiative forcing calculation using the full physical SBDART-derived BC TOA forcing outputs:

- Linear model: Mimicking the community's approach of scaling TOA with AOD at 550nm for total aerosol DRF (Matus et al., 2019; Sena et al., 2013; Sena and Artaxo, 2015), we derive a regression slope (β) between SBDART-generated BC TOA forcing and BC_{AOD550}.

$$TOA_{BC} \sim BC_{AOD550} \cdot \beta$$

- Parametric multiple linear regression (MLR) model: Expanding on the previously proposed MLR equation (Tiwari et al., 2023) we incorporate additional predictors; column mass (M_c) and number concentration (N_c), BC size, and mixing state along with BC_{AOD550} into the MLR framework

$$TOA_{MLR} = \alpha_0 + \alpha_1 . BC_{AOD550} + \alpha_2 . N_c + \alpha_3 . M_c + \alpha_4 . BCsize + \alpha_2 . \text{mixing state}$$

- Machine learning (ML) model: While MLR improves TOA prediction by accounting for additional variables, it assumes fixed, first order or pseudo-linearized, additive contributions of predictors (Cohen & Prinn, 2011). The ensemble learning algorithm herein employs a random forest approach, which helps explore the complex relationships and inter-

dependencies between the predictors and physically derived TOA, providing a more robust framework for BC TOA estimation.

210 Specifically, each region's RTM output BCTOA is subjected to a 70-30 train-test split, with 70% of the data used to train the model and 30% withheld as an independent test set. This approach allowed the model to learn relationships between predictors and TOA while ensuring a robust evaluation on unseen data. Beyond prediction, the ML approach also provides crucial insights into the relative importance of predictors in determining TOA forcing. The statistical metrics (R^2, MBE, MAE and RMSE) for both the training and test data are presented, along with the corresponding predicted vs. actual plots for each set along with

215 their statistics and error metrics provided in Supplement Figure S1 and Supplement Table S1 respectively. The ML-model demonstrated robust predictive capabilities in analyzing the relationship between BCTOA and key predictors in both Xuzhou and Dhaka, with R^2, RMSE, and MAE of 0.97, 1.7 W m^{-2}, and 1.1 W m^{-2} respectively on the training set and 0.96, 1.8 W m^{-2}, and 1.2 W m^{-2} respectively on the test set, capturing approximately 96% of the variance in BCTOA in Xuzhou. Similarly, in Dhaka, the model achieved an R^2, RMSE, and MAE of 0.96, 1.5 W m^{-2}, and 1.1 W m^{-2} respectively for the training and set and

220 0.96, 1.6 W m^{-2}, and 1.1 W m^{-2} respectively for the test dataset. In all cases, the MBE remained near zero, indicating negligible bias. Cross-validation using a 5-fold split yielded a mean R^2 of 0.96 with a standard deviation of 0.001, reflecting the model's consistency across different training subsets. Additionally, the learning curve analysis observed converging curve for RMSE as the datasets were added in subsequent runs, with training and validation curve closely converging. These metrics and observations assure confidence to apply the trained model across all the datasets and subset of these datasets under varying

225 conditions.

Currently, to the best of our knowledge, no observational products directly quantify BCTOA DRF while fully accounting for dynamic BC microphysics and using multi-wavelength optical properties in tandem. Although satellite and ground-based platforms provide key aerosol optical parameters (e.g., AOD, AAOD and SSA), they do not provide BC specific TOA DRF for direct comparison. Therefore, we use physically based COSMO-RTM model outputs, that accounts for BC microphysics

230 and optical properties, as the reference standard to compare our surrogate models. This ensures validation against a comprehensive, physically consistent benchmark in the absence of direct observational data. Furthermore, to better understand how different predictors influence TOA forcing, each surrogate model is tested across different pollution and morphological regimes. Pollution conditions were categorized based on BCAOD$_{550}$ values, while different morphological regimes were categorized based on BC size and mixing state (ratio of BC core size to total size) conditions. These conditions were generated

235 following percentile-based division as shown in Supplement Table S2. A series of performance and error metrics (adj R^2, root mean square error (RMSE), mean Absolute and bias error, mean absolute percentage error (MAPE), bias-corrected RMSE and confidence intervals etc.) are computed and compared, to assess the performance of different models detailed in.

2.3 SHAP (SHapley Additive exPlanation) Analysis

240 To further explain the feature contributions, Shapley Additive Explanations (SHAP) analysis is used, where SHAP values, derived from cooperative game theory (Lundberg and Lee, 2017), quantify the contribution of each feature by considering all possible combinations. These values capture both individual and joint feature contributions, offering a fair and consistent

explanation of the model's predictions. Additionally, violin plots are employed to visualize the distribution of SHAP values across predictions, providing insights into how feature contributions vary.

245

2.4 Testing ML models transferability: cross-regional and combined approach

Finally, to test if developed surrogate ML models can serve as a fast BC radiative transfer tool in other geographic regions, a cross-regional and combined model testing analysis was carried out. First, the ML model generated in one region (e.g., Dhaka) was applied to predict TOA in the other region (e.g., Xuzhou), and vice versa. The specific cross-regional model (ML*)

250   validation tested the transferability of region-specific models informed by local BC properties into different regions with their own unique local BC properties, providing critical insights into the extent to which these models perform across distinct environmental, microphysical, and total column conditions using the same sets of predictors. Additionally, a combined model (ML**) was developed by implementing stratified regional testing, combining data from both the regions as inputs, hence learning the variability in how TOA is physically computed based on relationships using predictors based on environmental

255   conditions across both regions in tandem. Subsequently ML** is again tested over both Xuzhou and Dhaka and is compared with SBDART TOA. The conceptual overview of this framework is summarized in Figure 2.
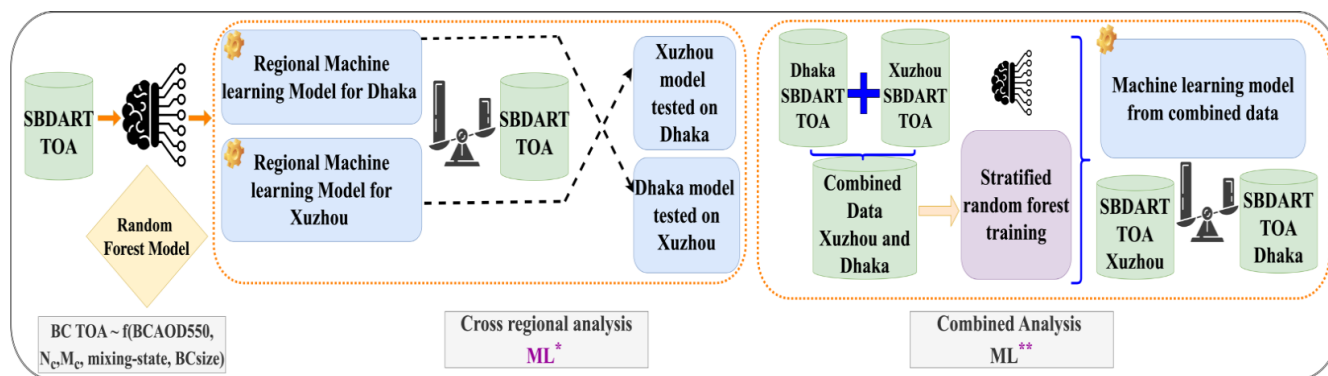
Figure 2: Conceptual schematic for conducting cross-regional (ML*) and combined (ML**) analysis

Finally high resolution (0.05° x 0.05°) climatological maps of SBDART, ML* and ML** BCTOA were generated and spatial

260   correlation are analyzed to assess how well the surrogate models capture spatial variability over a long-term average time frame. Additionally, comparison between the local ML and the ML** model is performed over these spatial aggregated climatologies, by computing error improvement metrics and spatial difference in absolute prediction errors evaluated against SBDART.

3 Results

3.1 Comparative analysis of black carbon microphysical, physical optical and properties in Xuzhou and Dhaka: Key predictors of TOA DRF

Optical, microphysical and column abundance properties like BCAOD, BC size (radius in nm) and mixing state (ratio of BC size to total size), N_c, M_c, BC core size directly or indirectly influence aerosol-radiation interactions, ultimately impact TOA forcing. Figure 3, below presents the r distribution of these parameters via probability density plots over both the regions.
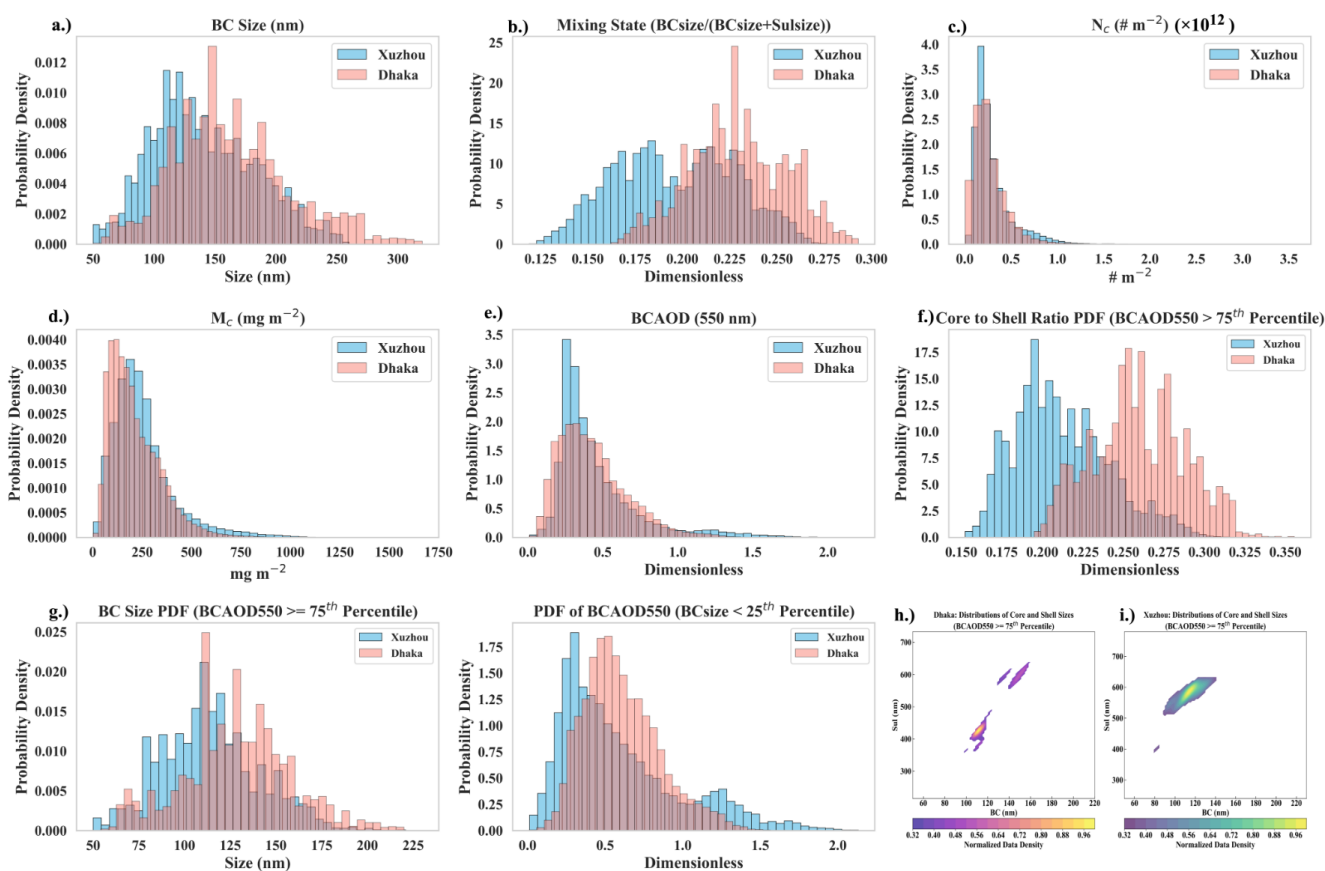
Figure 3: Probability density distributions of key predictors for aerosol radiative forcing analysis in Xuzhou and Dhaka: a.) Black Carbon (BC) core size, b.) Mixing state (ratio of BC size to total size), c.) Number column density (N_c), d.) Total mass column density (M_c), and e.) BCAOD at 550 nm, f.) BC core to Sulfate shell size ratio and g.) BC core size for polluted condition (BCAOD$_{550}$>75th percentile) h.) and i.) most prominent size distribution observed over Xuzhou and Dhaka during polluted days.

10

The regional differences in per-particle BC size and mixing state between Dhaka and Xuzhou revealed contrasting behavior. First, BC size showed a broader and mostly higher range in Dhaka (from 50 to 320 nm, with mean/25th/50th/75th percentiles distributed as 162.5/130/156/190 nm) than in Xuzhou (from 50 to 260 nm, with corresponding statistics of 140.5/110/134.4/170 nm). The mixing state distribution was also distinct, with the value over Dhaka both narrower and higher (from 0.16 to 0.29 with mean/25th/50th/75th observed as 0.23/0.21/0.23/0.25) than over Xuzhou (0.12 to 0.28, with corresponding statistics of 0.2/0.17/0.2/0.22). In general BC aerosols over Xuzhou are emitted as smaller particles which then more rapidly coat, while over Dhaka, larger BC cores are emitted and the coating is lesser. These results are consistent with the wide range of co-emitted sources and higher in-situ secondary aerosol and other atmospheric processing occurring in Xuzhou, and the less efficient combustion leading to more and larger soot monomers combined with less oxidative atmosphere in Dhaka leading to less overall secondary aerosol production. These factors play a crucial role in shaping the microphysical properties of BC, and subsequent influence on the solar radiation stream and overall atmospheric effects.

N_c exhibited distinct distribution patterns with the value in Xuzhou generally higher on average but less extreme (from 6.4×10^9 to 2.7×10^{12} #m^{-2}, with the mean/25th/median/75th values distributed as $3.0 \times 10^{11}/1.6 \times 10^{11}/2.3 \times 10^{11}/3.5 \times 10^{11}$ #m^{-2}) than in Dhaka (from 4.5×10^9 to 3.6×10^{12} #m^{-2}, with corresponding statistics $2.7 \times 10^{11}/1.5 \times 10^{11}/2.2 \times 10^{11}/3.5 \times 10^{11}$ #m^{-2}). Xuzhou exhibits a consistently higher baseline for N_c, as indicated by its minimum, 25th percentile, and median values, consistent with more sustained yet regulated aerosol sources from known industrial and urban centers, as well as influence from substantial regional transport. Dhaka shows slightly lower mean and baseline values, although its maximum N_c is substantially higher, highlighting the occurrence of extreme aerosol loading events, which are consistent with strong yet episodic sources, including extensive contributions from biomass burning, and brick kiln operations, as well as influence from stagnant atmospheric conditions, which exacerbate aerosol accumulation in the region(Rahman et al., 2019; Salam et al., 2021; Zaman et al., 2023). Interestingly, the 75th percentile values of N_c are comparable across both regions indicating similar levels of moderately high loading.

M_c exhibited a broader range and higher loading across all percentiles in Xuzhou compared to Dhaka. Over Xuzhou, M_c ranged from 2.8 to 1668.2 mg m^{-2} with mean/25th/median/75th values of 254.2/151.8/222.1/309.6 mg m^{-2}, while over Dhaka M_c ranged between 1.9 to 1052 mg m^{-2} with corresponding values of 211.9/113.3/181.2/284.9 respectively. This is concordant with a previous study which pointed out that the higher M_c in Xuzhou is mostly associated with the larger aerosol coating compared with Dhaka (Tiwari et al., 2025). This discrepancy is consistent with lower combustion efficiency in Dhaka and significant influences of agricultural and biomass burning, leading to larger cores but also slower secondary aerosol growth. Additionally, such conditions lead to reduced local solar radiation required for rapid secondary aerosol production of inorganic aerosols compared to Xuzhou. In contrast, Xuzhou's elevated BC levels are attributed to its higher total power consumption and diverse industrial emissions, which arise from both local and regional transport activities. This finding is consistent with observations from other urban and suburban regions throughout central and western China, where diverse emission sources, effective secondary aerosol formation processes, and significant co-emissions have been identified as contributing factors (Liu et al., 2024c). Consequently, these long-range transport events in Xuzhou may also further contribute to the higher M_c.

Notably, BCAOD at 550nm showed comparable values between Xuzhou and Dhaka, ranging from 0.01 to 2.2 with mean/25th/median/75th values distributed as 0.5/0.3/0.4/0.5 in Xuzhou and 0.4/0.3/0.4/0.6 in Dhaka. Detailed comparison reveals distinct regional differences in BC dynamics, with Xuzhou experiencing more extreme aerosol events contributing to BC loading, as reflected by its higher maximum and elevated mean values. These episodic events likely enhance the BC

315 loading and aging, in turn enhancing net extinction from inorganics, contributing to the longer tail in the distribution. In contrast, Dhaka exhibits a more uniform distribution of moderately high values, as evidenced by its slightly higher 75th percentile but lower overall maximum, suggesting high but consistent aerosol loading, potentially driven by continuous emissions from urban and regional sources. The elevated $BCAOD_{550}$ in Xuzhou is likely influenced by both local emissions and regional loading, as supported by Qin et al., (2022), which observed transported aloft aerosols promote rapid formation of secondary inorganics

320 like secondary sulfate over Xuzhou, which when coated with BC cores can enhance the overall extinction. Additionally, Chen et al., (2019) previously reported high BC to PM ratio in Xuzhou often associated with both southern and northern winds originating from major economic areas in the lower Yangtze River Delta and Beijing-Tianjin-Hebei provinces. Source attribution has pointed to Shandong as well as central provinces, Henan and Anhui, as significant contributors to BC loading over Xuzhou.

325 Further analysis of high polluted conditions ($BCAOD_{550}$>75th percentile) demonstrates distinct BC core size distributions. Xuzhou shows a compact distribution with BC cores mostly between 100–120 nm and sulfate shells of 500–600 nm, plus a smaller cluster of 80-90 nm cores with 390-410 nm shells, indicating well-coated small to medium cores. Dhaka's primary cluster features 100-120 nm cores with 390-450 nm shells, and a secondary cluster of larger 140–160 nm cores paired with 550-620 nm shells. The BCAOD probability density function for small cores associates these sizes with elevated pollution in

330 both areas, while core-to-shell ratios highlight a dominance of thicker shell coatings in Xuzhou, reflecting strong secondary inorganic formation. Conversely, Dhaka's narrower small-core distribution and larger core-to-shell ratios imply frequent pollution events involve larger BC cores with relatively thinner coatings. These contrasts emphasize secondary inorganic growth drives Xuzhou's polluted conditions, while primary emissions drive Dhaka's polluted conditions.

335 **3.2 Evaluating model Performance: Overall, and across varied pollution condition and morphological regimes**

The ML-model, MLR, and linear models reproduce the SBDART-derived TOA radiative forcing (mean: Xuzhou = -17.2 ± 9.2 W m^{-2}; Dhaka = -15.1 ± 7.7 W m^{-2}) with moderate-high fidelity, as evidenced by near-identical means and low percentage errors (ML: 7.8–8.5%; MLR: 13.0%; Linear: 16.0–20.4%). However, the ML-model exhibits superior accuracy, with the lowest RMSE (Xuzhou: 1.7 W m^{-2}; Dhaka: 1.5 W m^{-2}) and highest R^2 (0.96–0.97), reflecting its improved capacity to capture

340 non-linear BC-radiation interactions. The linear model underestimates extreme TOA values (e.g., Xuzhou 1st percentile: Linear = -49.0 W m^{-2} vs. SBDART = -45.3 W m^{-2}), while ML-model closely matches SBDART distributions (Xuzhou 1st percentile: ML = -43.9 W m^{-2} vs. SBDART = -45.3 W m^{-2}), particularly at tails. In Dhaka, ML's narrower 95% confidence intervals (-0.002 to 0.009 W m^{-2}) and lower MAE (1.1 W m^{-2}) highlight its robustness in capturing TOA variability. Both regions show systematic model divergence at warming conditions, where linear and MLR models underestimate warming (e.g., Xuzhou 99th

345   percentile: Linear = -7.2 vs. SBDART = -4.1 W m^{-2}), whereas ML marginally minimizes bias (ML = -4.5 W m^{-2}). The

performance of the Linear estimation, MLR, and ML models in predicting SBDART TOA were visualized through 2D density

plots along with the PDF distribution for both Xuzhou and Dhaka (Figure 4). The density plots show the relationship between

the predicted TOA (for each model) and the physical model (SBDART TOA), with color density indicating the concentration

of data points.

350
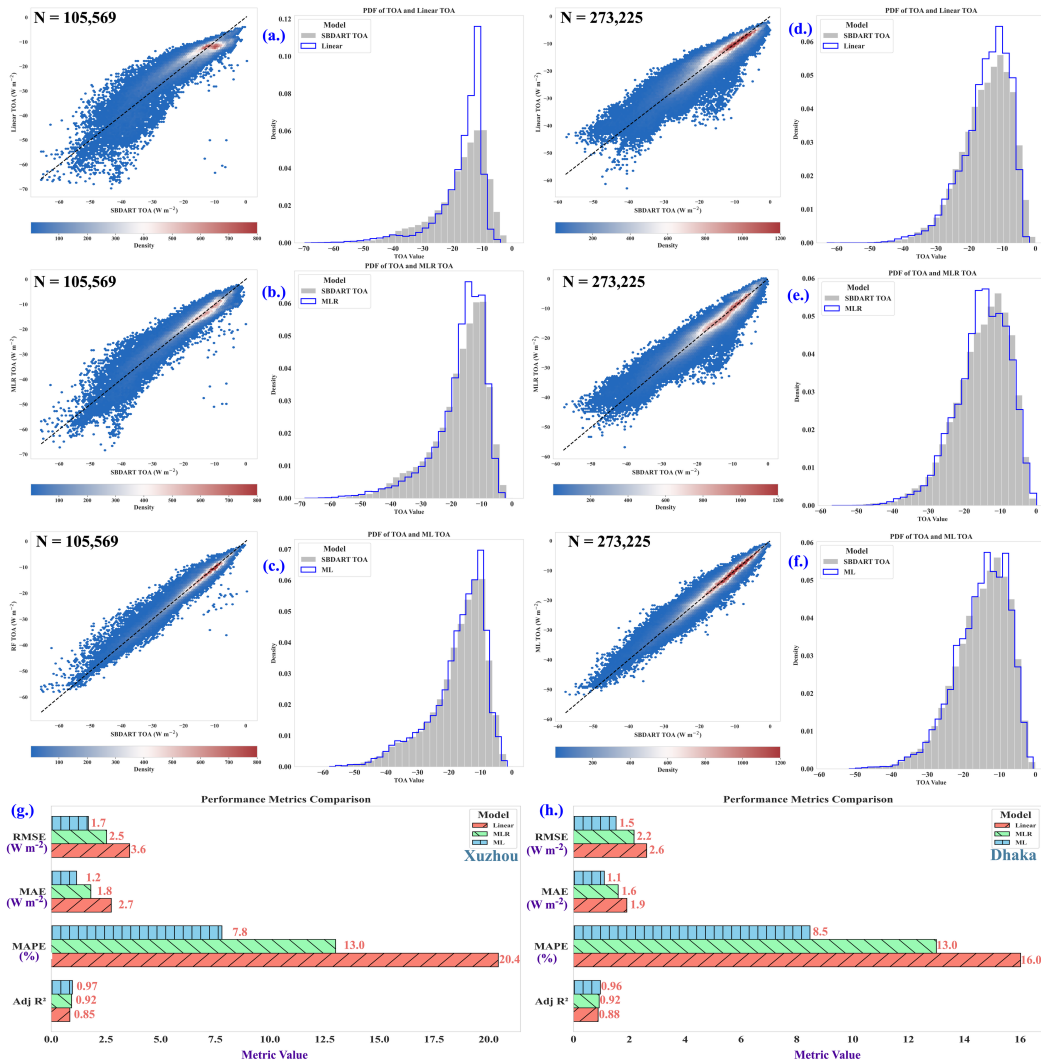
Figure 4: Comparison of BCTOA predictions from various models (Linear, MLR, and ML) with SBDART TOA for Xuzhou and Dhaka. The scatter plots (top row) display the relationship between model predictions and SBDART values, with color maps indicating the density of data points. The histograms (bottom row) show the probability density

355   **functions (PDFs) of BCTOA values from both SBDART and the models.**

The ML, MLR, and linear models exhibit distinct performance patterns across BCTOA radiative forcing regimes, revealing significant variations in accuracy, precision, and robustness. In Xuzhou, the linear model exhibited the highest errors in all TOA categories, with a mean error of 1.98 W m^{-2} (95% CI: 1.92–2.03) in Low TOA (more cooling scenarios) and -2.9 W m^{-2} (95% CI: -2.89 to -2.83) in High TOA (more warming scenarios), alongside persistent bias (RMSE = 3.4 W m^{-2} in High TOA).

360   The MLR model showed intermediate performance, reducing errors compared to linear (e.g., MAE = 2.8 W m^{-2} in Low TOA vs. Linear's 4.4 W m^{-2}) but still underperforming ML (MAE = 1.6 W m^{-2}). In High TOA, MLR's bias corrected RMSE (1.8 W m^{-2}) matched Linear's, indicating unresolved bias, while ML achieved the lowest RMSE and bias corrected RMSE (1.2 W m^{-2} and 1.1 W m^{-2}) and highest R^2 (0.73). In Dhaka, similar trends emerged but with smaller errors. Linear model had a mean error of 1.1 W m^{-2} in Low TOA and -1.2 W m^{-2} (95% CI: -1.2 to -1.1) in High TOA, with RMSE and bias corrected RMSE as

365   3.5 and 3.3 W m^{-2} and 2.0 and 1.6 W m^{-2} in Low and High TOA scenarios. MLR improved over Linear (e.g., MAE = 2.1 W m^{-2}in Low TOA vs. Linear's 2.8 W m^{-2}) but lagged behind ML (MAE = 1.5 W m^{-2}). In High TOA, MLR's R^2 (0.58) was higher than Linear's (0.47) but lower than ML's (0.78), with ML achieving the lowest RMSE (1.0 W m^{-2}).

An interesting pattern is observed over the range of TOA values transitioning between strong cooling and slight cooling/warming, hereafter considered the transition-TOA region. For both Mid-Low and Mid-High categories, all the models

370   demonstrated lower R^2 despite similar or lower error metrics than the Low and High TOA across some models. In both Xuzhou and Dhaka, the Mid-Low and Mid-High TOA categories revealed a striking inconsistency between error metrics and variance explained. For instance, in Xuzhou's Mid-Low category, the ML model achieved a low MAE of 1.1 W m^{-2} and RMSE of 1.6 W m^{-2}, comparable and better to its performance in extreme TOA ranges (e.g., Low TOA: MAE= 1.6 and RMSE= 2.4 W m^{-2} and High TOA: MAE = 0.9 W m^{-2}, RMSE = 1.2 W m^{-2}). Similarly, in Dhaka's Mid-Low category, ML had MAE = 1.2 W m^{-2} and RMSE = 1.6 W m^{-2}, better than its performance in the low TOA range (MAE = 1.5 W m^{-2}, RMSE = 2.0 W m^{-2}). However,

375   ^{2} and RMSE = 1.6 W m^{-2}, better than its performance in the low TOA range (MAE = 1.5 W m^{-2}, RMSE = 2.0 W m^{-2}). However, R^2 values in mid-range categories were significantly lower (e.g., Xuzhou Mid-Low; R^2 = 0.56 vs. High TOA: R^2 = 0.73 and Low TOA: R^2 = 0.89; Dhaka Mid-Low: R^2 = 0.50 vs. High TOA: R^2 = 0.78 and Low TOA: R^2 = 0.87). This pattern persisted across models. In Xuzhou's Mid-High category, MLR exhibited a mean error near zero (-0.4 W m^{-2}) but explained only 26% of variance, while linear model had a 11.9% MAPE; lower than Low and High TOA category, but R^2 of 0.13. In Dhaka's Mid-

380   High category, MLR achieved a low MAPE of 13.2% when R^2 was 0.33, compared to its performance at High TOA (MAPE = 21.5% R^2 = 0.58). These results highlight a bias-variance trade-off, meaning, the models tend to capture the average radiative forcing magnitude fairly well (low RMSE/MAE) but failed to explain data variability in mid-range TOA conditions. This discrepancy likely arises from the complex, non-linear interplay of aerosol microphysics and atmospheric dynamics that dominate the transition between cooling to warming TOA condition, as well as daily-scale variability which occurs underlying

385   these special events as they crossover from one regime to the other. For instance, transient processes such as mixing-state evolution (e.g., sulfate coating on BC cores (Cappa et al., 2012; Fierce et al., 2020); gradual growth in per particle size and mass (McFiggans et al., 2006), and impacts of changes in precursor species on the size distribution (Seinfeld et al., 2003)), can introduce high intra-category variability, or spatial and temporal variation, which linear and MLR framework cannot resolve and ML only partially captures. These regimes also involve competing absorption-scattering balances, where minor shifts in

390 aerosol composition or morphology disproportionately alter per-particle properties (Guan et al., 2025) and even forcing directionality, amplifying unexplained variance (Samset et al., 2018b).

To assess the model performance under different environmental and microphysical conditions, performance comparison across different mixing state and BC core size conditions were analyzed and tabulated in Table 1.

Table 1. Performance Table of Linear, MLR and ML model assessed across different BC core size and mixing state
395 **conditions. Metrics like Adj R^2, and errors (RMSE, MAE, MBE and MAPE) are used for model robustness comparison across different morphological regimes.**

Coating	Metrics	Xuzhou			Dhaka		
		Linear	MLR	ML	Linear	MLR	ML
	N	26121	26121	26121	66327	66327	66327
	Adj R^2	0.83	0.91	0.97	0.76	0.86	0.93
	RMSE	4.6	3.3	1.9	3.5	2.7	1.9
Heavily	MAE	3.6	2.5	1.2	2.8	2.0	1.4
Coated	MBE	2.2	-0.02	0.10	1.4	0.3	0.05
	MAPE	15.2	14.5	5.1	12.1	9.4	6.5
	N	26472	26472	26472	68746	68746	68746
	Adj R^2	0.78	0.88	0.94	0.79	0.84	0.89
	RMSE	3.5	2.6	1.9	2.3	2.1	1.7
Moderately	MAE	2.4	1.8	1.3	1.8	1.6	1.3
Coated	MBE	1.2	0.1	-0.01	0.3	-0.07	0.01
	MAPE	11.4	9.7	6.6	11.3	10.7	8.2
	N	25734	25734	25734	67912	67912	67912
	Adj R^2	0.71	0.80	0.88	0.62	0.72	0.90
	RMSE	2.6	2.1	1.7	2.7	2.3	1.4
Minimally	MAE	1.9	1.6	1.2	1.8	1.7	1.0
Coated	MBE	-0.6	0.07	-0.02	-0.9	-0.7	-0.03
	MAPE	14.3	12.1	8.5	16.5	15.7	9.1
	N	27242	27242	27242	70240	70240	70240
	Adj R^2	-0.20	0.69	0.81	0.77	0.82	0.92
	RMSE	3.4	1.7	1.4	1.7	1.5	1.0
Barely	MAE	3.0	1.4	1.0	1.3	1.1	0.7
Coated	MBE	-2.7	-0.1	-0.05	-0.7	0.5	-0.02

BC core size	Metrics	Linear	MLR	ML	Linear	MLR	ML
	MAPE	40.0	15.7	11.0	23.9	16.1	10.0
	N	26188	26188	26188	66312	66312	66312
	Adj R^2	0.85	0.92	0.98	0.88	0.93	0.96
	RMSE	4.2	3.1	1.7	2.6	2.0	1.4
Small	MAE	3.1	2.3	1.1	1.9	1.5	1.0
	MBE	1.0	-0.3	0.05	0.6	0.01	0.01
	MAPE	13.8	15.4	4.9	8.8	7.4	5.0
	N	26596	26596	26596	70155	70155	70155
	Adj R^2	0.82	0.91	0.96	0.88	0.92	0.96
	RMSE	3.8	2.7	1.7	2.5	2.1	1.5
Medium	MAE	2.8	1.7	1.1	1.8	1.5	1.1
	MBE	1.3	0.3	-0.01	0.1	0.2	-0.01
	MAPE	13.6	8.7	5.7	10.8	9.2	6.7
	N	25368	25368	25368	66214	66214	66214
	Adj R^2	0.80	0.87	0.92	0.78	0.84	0.89
	RMSE	2.8	2.2	1.8	2.6	2.2	1.8
Big	MAE	2.2	1.6	1.2	2.0	1.7	1.3
	MBE	0.2	0.3	-0.01	0.5	0.2	0.03
	MAPE	14.9	10.5	8.1	14.0	12.5	9.2
	N	27417	27417	27417	70544	70544	70544
	Adj R^2	0.29	0.74	0.84	0.47	0.60	0.87
	RMSE	3.4	2.1	1.6	2.8	2.4	1.4
Very Big	MAE	2.9	1.6	1.2	2.0	1.7	1.0
	MBE	-2.4	-0.2	-0.02	-1.2	-0.4	-0.02
	MAPE	38.6	17.2	12.3	29.9	22.5	12.8

p-value < 0.05; performance metrics for Dhaka are represented in italicized format.

For heavily coated BC, ML achieves superior accuracy in both Xuzhou (Adj. R^2 =0.97) and Dhaka (Adj. R^2 = 0.93), reducing

400   RMSE by 59% and 46% relative to linear and MLR models, with near-zero mean bias (MBE: 0.1 vs. 2.2 in Xuzhou; 0.05 vs. 1.4 in Dhaka). Under moderately coated conditions, ML remains dominant, lowering MAE 46–50% in Xuzhou (1.3 vs. 2.4 W

16

m^{-2}) and MAPE by19–24% in Dhaka (8.2% vs. 10.7%). Even for minimally coated BC, ML demonstrates strong predictive skills, reducing RMSE by 35% compared to MLR over Xuzhou and lowering MAPE by 42% in Dhaka. Notably, for barely coated BC, linear modeling fails entirely in Xuzhou (Adj. R^2 = -0.20), whereas, ML retains robust performance (Adj. R^2: 0.81,

405   RMSE: 1.4 W m^{-2}, MAPE: 11.0%), underscoring its resilience under low-coating conditions. In Dhaka, ML's MAPE (10.0%) reducing MAPE by 38% lower than MLR's (16.1%), with near-perfect bias neutrality (MBE -0.02). Linear and MLR models exhibit stronger systematic bias in these regimes including underprediction (MBE: −2.7 W m^{-2}) in Xuzhou, and slight overprediction (MBE: 0.5 W m^{-2}) in Dhaka. Regarding BC core size, ML achieves high precision for small cores in both cities (Adj. R^2= 0.98/0.96, RMSE= 1.7/1.4 W m^{-2} MAPE= 4.9%/5.0% in Xuzhou/Dhaka, reducing RMSE errors by 45%-60% over

410   Xuzhou and 30-46% over Dhaka compared to MLR and linear models. Transitioning to very big BC cores, the linear frameworks perform poorly in Xuzhou (Adj. R^2 = 0.29; MAPE= 38.6%), while ML retains robust accuracy (Adj. R^2 = 0.84, MAPE= 12.3%). In Dhaka, ML reduces RMSE by 42% and nearly halves MAPE relative to MLR. Similarly, model performances across different pollution conditions also demonstrates superior accuracy and robustness of ML compared to its contemporaries; detailed evaluation including Taylor diagram analysis in Supplement Figure S2 within Supplement section

415   S2.

Analysis of the underlying microphysical properties reveals that ensemble learning models consistently outperform linear and MLR approaches in reproducing BCTOA, across diverse pollution conditions (clean to polluted), mixing states (heavily coated to barely coated), and size categories (small to very large) in both Xuzhou and Dhaka. Statistically, RF achieves superior accuracy (Adj. R^2 spanning 0.73-0.98), near-neutral bias (|MBE| ≤ 0.1), and error reductions of 30-67% (RMSE) compared to

420   linear models, with performance gaps widening under complex conditions-such as heavily polluted scenarios (Xuzhou: RF RMSE 2.26 W m^{-2} vs. MLR 3.62 W m^{-2}) or minimally coated BC (for Dhaka; RF MAPE 9.1% vs. MLR 15.7%). Physically, ML's dominance stems from its ability to resolve non-linear interactions between BC core size, coating thickness, and atmospheric aging processes, which linear frameworks oversimplify, including the transition states between negative and nearly zero or even positive TOA. The observed bias-variance trade-off in mid-range TOA categories further underscores the

425   complex interplay of BC microphysics and atmospheric dynamics and other sources of non-linearities which ML models partially capture but remains a challenge for conventional approaches.

3.3 Interpreting BC forcing drivers using SHAP Analysis of ML

To interpret and quantify the contribution of individual predictors to the BCTOA radiative forcing, we applied Shapley

430   Additive exPlanations (SHAP) analysis. This analysis provides a model-agnostic measure of how variations in BC optical, microphysical, and column properties influence the predicted TOA forcing under contrasting atmospheric and emission environments in Xuzhou and Dhaka (Figure 5), while explicitly accounting for non-linear feature interactions.
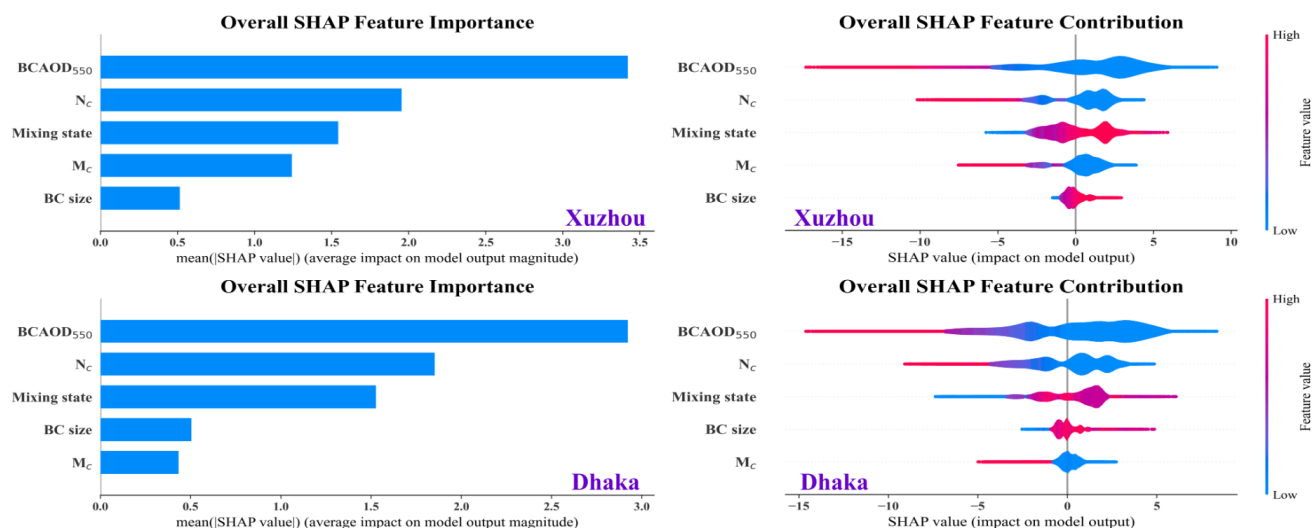
Figure 5: Overall feature importance and feature contributions for predicting BCTOA in Xuzhou and Dhaka. The bar plots (left panel) display the overall feature importance based on the mean SHAP value, and the violin plots (right panel) show the distribution of SHAP values for each feature, indicating the direction and magnitude of feature contributions to the model's output. Blue corresponds to low feature values, and red indicates high feature values, with the SHAP values reflecting the impact driving the BCTOA forcing towards warming and/or cooling.

Across both regions the ML models exhibit broadly consistent feature rankings, with $BCAOD_{550}$ emerging as the most influential predictor for BCTOA forcing. The mean SHAP associated with $BCAOD_{550}$ is larger in Xuzhou (3.4, 62.1% positive) than in Dhaka (2.9, 57.3% positive). However, SHAP distributions reveal pronounced non-linearity across TOA forcing regimes, with $BCAOD_{550}$ contributing positively under clean to moderately polluted conditions ($BCAOD_{550}$; 0.01-0.53), but increasingly negative under moderately to heavily polluted conditions ($BCAOD_{550}$; 0.37-1.9). This sign reversal in SHAP contributions reflects a transition in the modeled radiative response, wherein increases in total extinction and scattering enhancement outweigh absorption enhancement at higher aerosol loadings. The overlap region (0.37-0.53), where SHAP contribution spans both positive and negative, demonstrates column loading and total column extinction alone are not sufficient to determine TOA warming or cooling. Instead, the ML interpretation indicates that per-particle microphysical properties-represented here through dynamic coating ratios and BC core size, simultaneously modulate absorption, total scattering, and angular redistribution, producing regime-dependent forcing behaviour. This microphysics-driven TOA sign variability was demonstrated by Tiwari et al., (2023), while such non-linear interactions and sensitivity are often high AOD contributing to more negative TOA forcing is consistent with the total attenuation under the conditions where scattering enhancement is larger than the absorption enhancement, likely drive by the consideration of dynamic coating ratios and ranges, where non-linear changes in absorption, total scattering, and scattering angle occur simultaneously with small changes in the mixing ratio and core size in tandem as previously highlighted by Tiwari et al., (2023). In this context, the present SHAP analysis further reveals

that per-particle microphysics and overall column loading can each contribute either positively or negatively to TOA forcing, depending on their coupled state. This behaviour highlights that commonly used assumptions of external mixing and reliance on AOD alone are insufficient, as they may yield either enhanced scattering or absorption while systematically missing critical microphysical effects that govern the net TOA response In the range of AOD values between 0.37 and 0.53, the per particle

460   microphysics and overall column loading can contribute either positively or negatively to TOA forcing, suggesting that commonly used external mixing assumption and AOD in tandem are insufficient (Mahajan et al., 2013; Mehrotra et al., 2024, 2025), either yielding enhanced scattering or absorption, thus assessing and demonstrating BC mostly exerting a positive TOA missing actual microphysical effects.

Followed by $BCAOD_{550}$, N_c emerges as the second most important predictor in both the regions, with comparable mean SHAP

465   of (1.95 over Xuzhou and 1.85 over Dhaka). In Xuzhou, SHAP contributions from N_c are predominantly positive up to approximately the 50th percentile, while higher number concentrations ($> 65^{th}$ percentile) increasingly contribute to negative TOA forcing. Dhaka observes a similar finding, however with the range of N_c contributing positively to warming being narrower ($< 40^{th}$ percentile). While SHAP explains model sensitivity rather than emission source characteristics, this behaviour is consistent with BC populations that remain weakly mixed over a broader range of lower particle numbers in Dhaka,

470   indicative of limited microphysical aging and enhanced absorption efficiency. In contrast, the narrower range of N_c associated with positive TOA contributions likely suggests more rapid microphysical evolution, plausibly facilitated by co-emitted non-absorbing aerosols that promote condensation, coagulation, and coating growth.

The SHAP result further reveal a moderate but systematic role of mixing state in modulating the predicted BCTOA forcing. While the mean SHAP magnitude associated to mixing state is similar in both the regions (~1.5) the sign and distribution vary.

475   The distribution of SHAP values indicates that positive contributions occur more frequently in Dhaka (58.6%) than in Xuzhou (44.8%), reflecting differences in how mixing-state variability influences the modeled TOA response across the two urban regions. Higher mixing state values (≥0.21 in Xuzhou; ≥0.23 in Dhaka), corresponding to thinner coatings and/or larger BC core are generally associated with enhanced TOA warming, whereas, lower mixing states (<0.17 in Xuzhou, <0.16 in Dhaka), reflect thicker coatings and smaller core fractions, preferentially contributing to negative BCTOA (cooling) though increased

480   scattering. These regional contrasts highlight that mixing-state effects on BCTOA forcing are strongly context-dependent and emerge through interactions with column loading and particle number, rather than acting as an independent control.

In contrast, M_c and BC size exhibit comparatively weaker influence on predicted BCTOA forcing. In Xuzhou, M_c observes a higher mean SHAP than Dhaka (1.24 vs. 0.43), with only the upper ~31% of column mass loading (>450 mg m^{-2}) contributing to cooling. This is likely reflecting conditions, where scattering by co-emitted aerosols dominates absorption. In Dhaka, BC

485   core size marginally outweighs M_c in importance, though its overall contribution remains minimal, with only 9% of larger BC cores (>220 nm) weakly enhancing warming. This weak sensitivity suggests that, within the observed range, BC size variations exert a secondary influence compared to column optical extinction, abundance and mixing state.

When stratified across distinct TOA forcing regimes-from cooling to warming, SHAP analysis reveals that $BCAOD_{550}$, consistently exerts the largest influence on the predicted BCTOA forcing, while mixing state and N_c, provide a secondary but

490 systematic contributions with regime dependent importance. This evolving hierarchy of feature contributions highlights the strongly non-linear nature of aerosol impacts on TOA forcing, indicating that key transition behaviour is governed by coupled changes in column optical loading and per-particle microphysics, rather than by bulk optical properties alone. The detailed SHAP analysis across TOA regimes is presented in Supplement Figure S3 within Supplement section S3.

495 **3.4 Adaptability of cross-regional and combined ML surrogates under domain shift**

Understanding the cross-regional adaptability of ML models is critical for assessing their transferability in terms of predicting BCTOA over different regions from where the ML model was trained. The performance of the cross-regional ML models is evaluated by applying the Xuzhou-trained model to Dhaka data and vice versa. In parallel, model adaptability is evaluated by using combined model (ML**) surrogate trained on samples drawn from both the regions, and performing comparison with

500 region-specific ML surrogates with SBDART DRF as reference. This analysis revealed that the cross-regional application results in slight performance degradation while still retaining non-trivial predictive skill, as visualized in Figure 6.
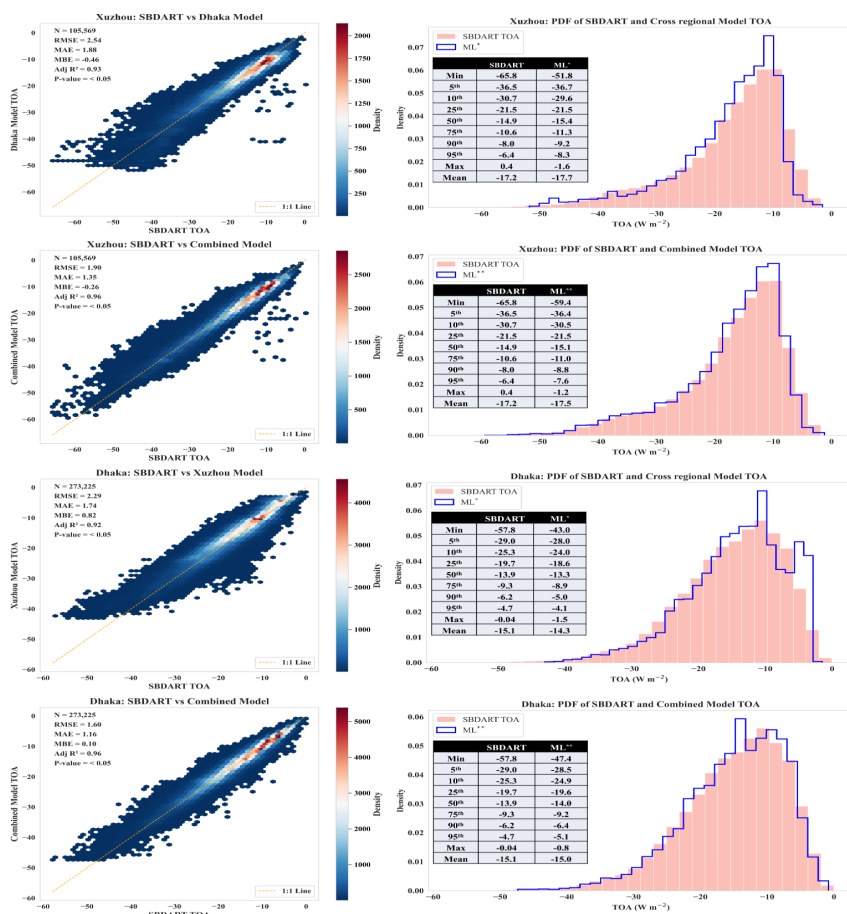

Figure 6: Comparison of SBDART-derived BCTOA forcing with cross-regional (ML*) and combined (ML**) ensemble learning models for Xuzhou and Dhaka. Left panels show scatter density plots of model-predicted BCTOA versus

505 **SBDART TOA, including key statistical metrics. Right panels present PDF comparisons between SBDART BCTOA and ML-predicted BCTOA, with statistical summaries of BCTOA distributions at different percentiles.**

Understanding When the Dhaka-trained ML model is applied over Xuzhou, the predicted BCTOA forcing remains strongly correlated with SBDART estimates (R = 0.96, p < 0.05), but exhibits reduced variability (predicted standard deviation = 8.7 W m^{-2} versus 9.2 W m^{-2}), indicating incomplete capture of Xuzhou's TOA extremes. This is accompanied by a systematic

510 negative bias (MBE = -0.46 W m^{-2}, 95% CI= -0.47 to -0.44), corresponding to an overestimation of cooling and an elevated RMSE (2.5 W m^{-2}), approximately 24% higher than that of the local Xuzhou ML model (RMSE = 1.9 W m^{-2}). The associated percentage error (14%) and residual standard deviation (2.5 W m^{-2} after bias removal) indicate the performance degradation arises from both reduced variance representation and systematic bias. These differences may primarily be linked to shifts in the distributions of BCAOD$_{550}$, N$_c$ and mixing-state, particularly exerting stronger modulation of BCTOA under warming

515 conditions. Conversely, employing the Xuzhou-trained ML model to Dhaka also retains high correlation (R = 0.96, p < 0.05) but underestimates TOA variability (predicted standard deviation = 7.3 W m^{-2} vs. observed standard deviation = 7.7 W m^{-2}) and systematically over-predicts warming in Dhaka (MBE = +0.82 W m^{-2}, 95% CI= 0.81 to 0.83). These inconsistencies likely stem due to the differences in BC microphysical regimes between the two regions, including variations in BC core size distributions and coating evolution, which are not fully captured when models are transferred across regions. Despite these

520 discrepancies, ML* models outperform local linear models, and performed comparably against the local MLR models. Over Xuzhou, Dhaka-trained model achieves a higher capability to capture variance (R^2=0.92) compared with local linear (R^2=0.85) and local MLR, with a 30% lower percentage error than linear (14.0% vs. 20.4%). Similarly in Dhaka, the Xuzhou-trained ML (R^2=0.91) surpasses local linear (R^2=0.88) and is similar to local MLR (R^2=0.92).

The combined ML** model, exhibits improved generalization across both regions with minimal loss of regional accuracy. In

525 Xuzhou, the combined model attains an Adj. R^2=0.96 (RMSE = 1.90 W m^{-2}, MAE = 1.4 W m^{-2}), closely matching the local ML model (R^2=0.97, RMSE = 1.70 W m^{-2} and MAE=1.2 W m^{-2}) while significantly outperforming local linear (RMSE = 3.6 W m^{-2} and MAE = 2.7 W m^{-2}) and local MLR (RMSE = 2.5 W m^{-2} , MAE = 1.8 W m^{-2}). Similarly, in Dhaka, the combined model achieves R^2=0.96 (RMSE = 1.6 W m^{-2}, MAE = 1.2 W m^{-2}), nearly equaling local ML (R^2=0.96, RMSE = 1.5 W m^{-2}) and surpassing local linear (R^2 = 0.88, RMSE = 2.6 W m^{-2}) and local MLR (R^2 = 0.92, RMSE = 2.2 W m^{-2}). Although the

530 combined model does not consistently outperform region-specific ML surrogates, it substantially reduces biases associated with cross-regional transfer.

3.5 Spatial climatological evaluation and robustness of the ML** model

Swath-by-swath pixel comparisons between the cross-regional (ML*) and combined (ML**) models provide insight into short-

535 term, local-scale predictability of BC radiative effects, but do not directly characterize the models' ability to reproduce long-term spatial structure and climatological variability. To assess regional climatology and spatial generalization, we therefore compare the 0.05° weighted BCTOA forcing climatology simulated by ML* and ML** against SBDART benchmarks. This spatial analysis serves two complementary purposes: to assess the fidelity with which each surrogate reproduces long-term

spatial patterns and climatological variability of BCTOA forcing (Figure 7), and (ii) to examine whether the improved cross-

540   regional adaptability of the ML** model translates into spatial performance relative to region-specific ML surrogates (Figure 8).
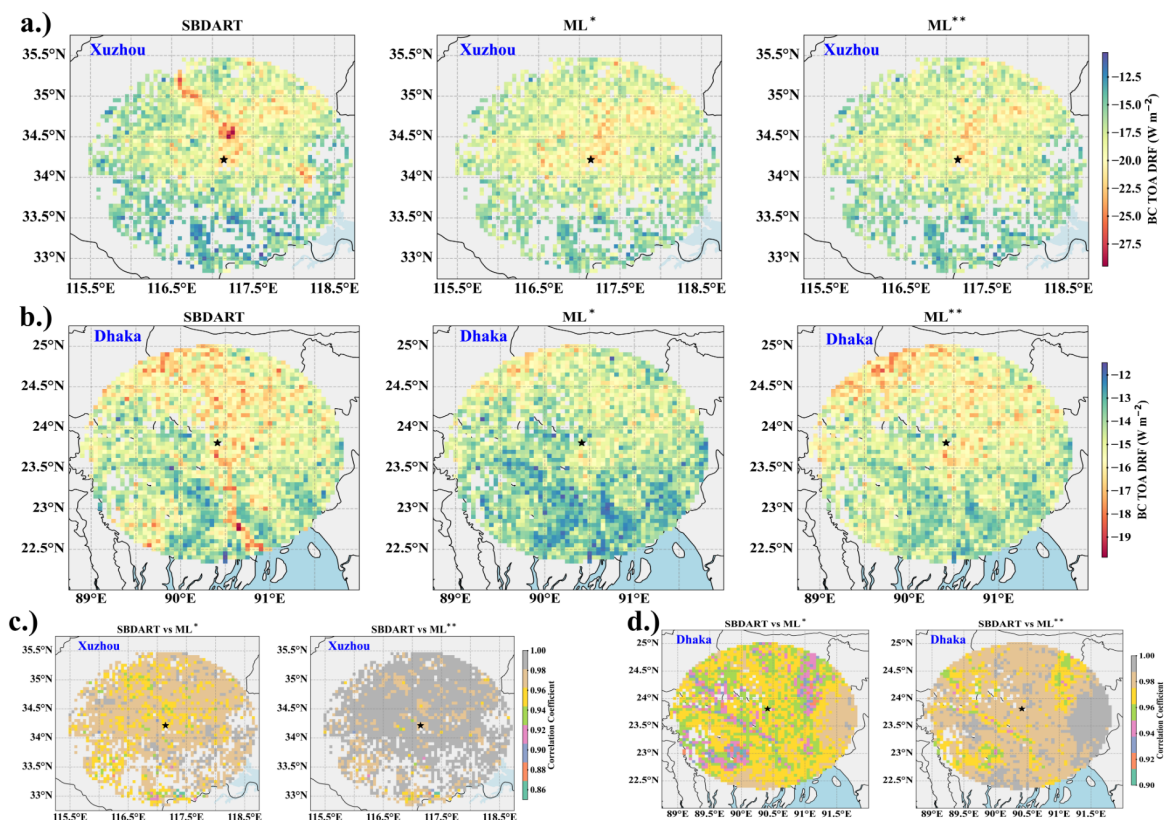
Figure 7: Spatial Evaluation of BCTOA DRF Simulations: Comparison of SBDART, Cross-Regional (ML*), and Combined Data (ML) surrogate ML models Over Xuzhou and Dhaka. Panels (a–b) show weighted climatology maps**

545   **of BCTOA DRF simulated by SBDART (reference model), cross-regional (ML*) model, and combined (ML**) model over Xuzhou (a) and Dhaka (b). Panels (c–d) present grid-by-grid correlation coefficients between SBDART and ML* and ML** for Xuzhou (c) and Dhaka (d). Color bars indicate TOA DRF values (W m^{-2}) and correlation coefficients. Stars mark key observational sites (SONET/AERONET stations) over Xuzhou and Dhaka respectively.**

Over Xuzhou (Figure 7a), both ML models capture the general spatial distribution of BC forcing, including the broad patterns

550   of cooling (negative forcing) over central and northern regions and warming (positive forcing) in the south. The overall mean BCTOA DRF simulated by SBDART across the domain was -17.4 ± 2.6 W m^{-2}, with ML* showing a mean of -17.8 ± 2.1 W m^{-2} and ML** at -17.6 ± 2.2 W m^{-2}. Despite this consistency in weighted climatological mean, localized discrepancies emerge in regions characterized by strong spatial gradients. Specifically, SBDART simulates an intense, spatially confined cooling feature north-northwest of the Xuzhou_CUMT station, which both ML* and ML** reproduce only in a spatially diffused form,

555   underestimating its magnitude and sharpness. This smoothing likely reflects a combination of spatial averaging, regularization,

and error propagation inherent to ML surrogates, which preferentially preserve coherent regional patterns while attenuating localized extremes. Over Dhaka (Figure 7b) differences between ML* and ML** become more pronounced. SBDART simulates a weighted climatological BCTOA mean of -15.0 ± 1.2 W m^{-2} closely matched by ML** (-14.9 ± 1.1 W m^{-2}), whereas ML* exhibits a weaker cooling (-14.3 ± 1.1 W m^{-2}). In terms of spatial coherence, ML** demonstrates superior

560   agreement with SBDART, particularly north of the Dhaka_University AERONET station, where SBDART resolves localized cooling pockets with sharp gradients. ML** preserves both the spatial extent and intensity of these features, while ML* underestimates their magnitude. Similarly, south of the station, SBDART indicates relatively warmer BCTOA forcing, which ML** reproduces with high fidelity, whereas ML* overestimates warming in these regions.

A shared limitation of both ML models is evident in their inability to fully reproduce a pronounced cooling pocket centered

565   near 90.5°–91° E and 22.5°–23° N. This feature, prominent in SBDART simulations, is absent in ML* and only feebly represented in ML**, suggesting that region-specific non-linear relationships between predictors and TOA forcing are not fully captured by cross-regional or combined training alone. Such discrepancies are consistent with a well-recognized trade-off in ML applications to atmospheric and environmental sciences; wherein spatial regularization improves overall coherence and reduces random noise but can smooth localized extremes and hotspots (Colin et al., 2018; Rasp et al., 2018; Reichstein et al.,

570   2019; Soriano Jr and Maxwell, 2023). Grid-by-grid spatial correlations further demonstrate that ML** consistently outperforms ML* across the majority of the domain in both regions (Figures 7c–d), achieving statistically significant correlations ($p < 0.05$) for more than 90% of grid cells.

Having established that ML** outperforms the cross-regional ML* in reproducing climatological spatial structure, we next evaluate its robustness relative to fully trained, region-specific ML models (Figure 8). This comparison assesses whether the

575   combined model can generalize across diverse BC microphysical and emission regimes without sacrificing local predictive skill.

In Xuzhou (Figure 8a), despite complex aerosol environments characterized by high BC column number density, more internally mixed particles, and varying BC core-to-total mass ratios, ML** achieves lower absolute error than the local ML model in approximately 32% of grid cells. These improvements are most evident over grids influenced by large industrial

580   sources, where spatial variability in scattering enhancement and coating evolution is pronounced. While ML** underperforms the local ML model in other parts of the domain, its overall accuracy remains robust (RMSE ~ 1.1 W m^{-2}; MAPE $\sim 4.5\%$). Over Dhaka (Figure 8c), ML** outperforms the local ML model over a larger fraction of the domain, achieving lower absolute error in 53.5% of valid grid cells. Spatially aggregated metrics indicate comparable performance between ML and ML**, with low bias and RMSE (~ 0.6 W m^{-2}) and similar MAPE ($\sim 2.8\%$), demonstrating that the combined model retains strong predictive

585   capability in a region dominated by distinct BC microphysical regimes.
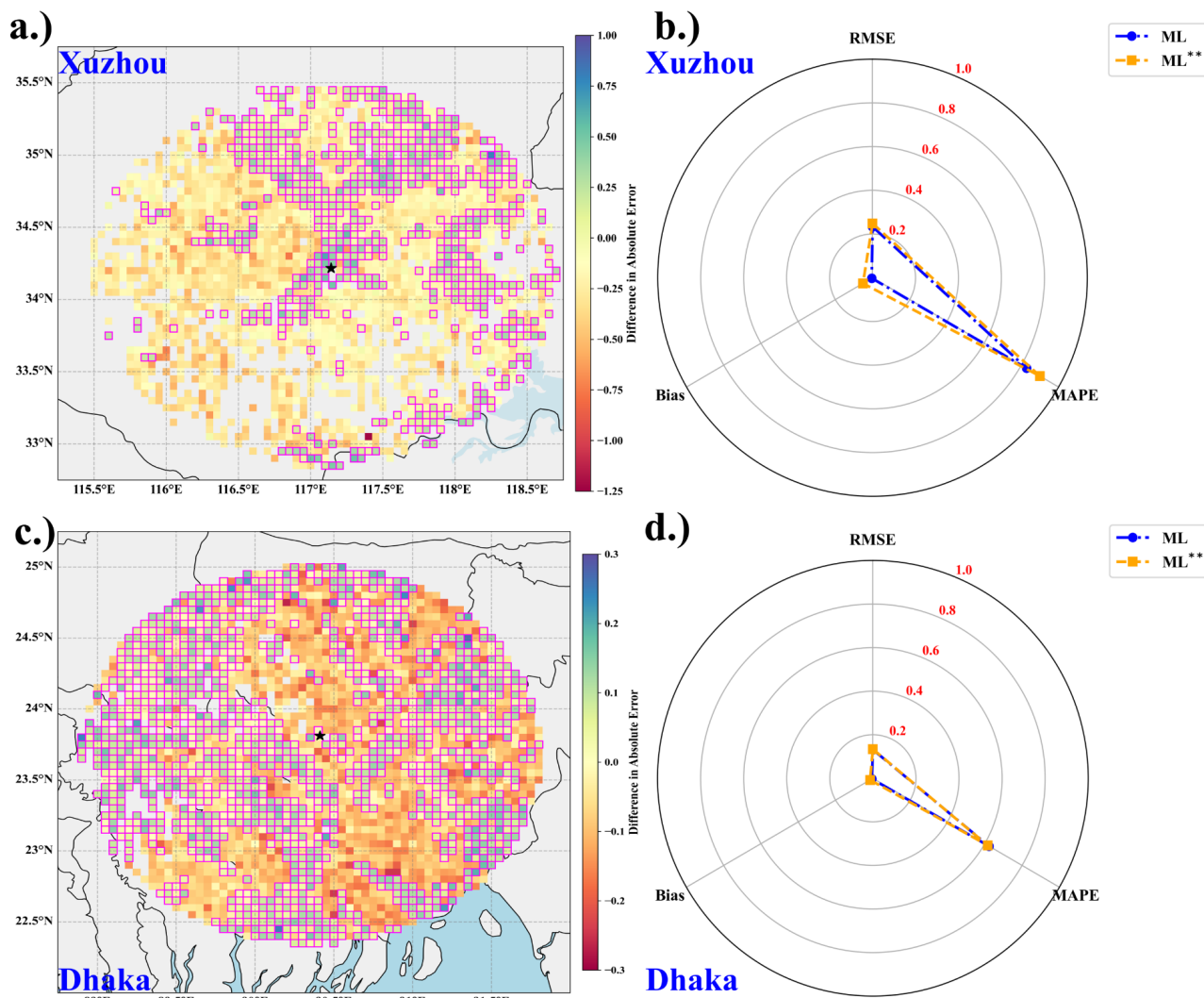
Figure 8: Spatial comparison of combined and region-specific ML performance. Panels (a) and (c) show maps of the difference in absolute error (|ML − SBDART| − |ML − SBDART|) over Xuzhou and Dhaka, respectively. Positive values indicate grid cells where the combined ML (ML**) yields lower absolute error than the region-specific ML model, while negative values indicate underperformance. Magenta-outlined grid cells mark locations where ML** achieves strictly lower absolute error. Panels (b) and (d) present radar plots comparing domain-aggregated performance metrics (RMSE, MAPE, and bias) for ML and ML** over Xuzhou and Dhaka, respectively. Metrics are normalized using min–max scaling, where 0 denotes the best observed performance and 1 the worst. Stars indicate SONET/AERONET sites.**

This grid-level behaviour is further reflected in the domain-aggregated performance metrics (Figures 8b and 8d). Over both domain RMSE, MAPE, and bias show that the ML** performs comparably to the region-specific ML model in both Xuzhou

24

and Dhaka, with no systematic degradation in any metric. In Xuzhou, ML** exhibits slightly higher bias than the local ML model, consistent with its underperformance in portions of the domain, while near similar RMSE and MAPE. In Dhaka, the two models show nearly identical normalized metrics, confirming that the ML** retains robust predictive skill while improving performance over a larger fraction of grid cells.

605 Overall, these results indicate that combined training enables ML** to capture substantial spatial variability and retain predictive skill across regions with contrasting BC microphysical-optical characteristics. While the combined model does not uniformly outperform region-specific surrogates, it achieves comparable or superior performance over substantial portions of both domains, supporting its utility as a unified framework for transferable BC radiative forcing estimation. At the same time, the results underscore an inherent trade-off between generalization and regional specificity; blending heterogeneous

610 distributions improves robustness to domain shifts but may partially dilute localized interactions that are optimally captured by region-specific models.

4 Conclusions

This study advances the COSMO framework by refining the characterization of black carbon (BC) microphysical and columnar properties derived in Tiwari et al., (2025) and integrating them into a large ensemble of physically consistent radiative transfer

615 simulations. By coupling observation-constrained microphysics with more than 370,000 RTM runs, we generate high-resolution estimates of BC direct radiative forcing (DRF) that resolve both spatial and temporal variability beyond what is achievable with conventional mass-based approaches.

A central scientific finding is the emergence of grid-scale BCTOA forcing that spans both positive and negative values within the same regional domains. While positive BCTOA is widely reported, the occurrence of negative BCTOA highlights the

620 importance of resolving microphysical and column-dependent absorption-scattering competition, which is inadequately represented in many current climate-model parameterization. This demonstrates that BC radiative effects are not monotonic with loading and that realistic aerosol-radiation interactions require explicit treatment of particle size, mixing state, and column abundance. The contrast between Xuzhou and Dhaka provides a compelling illustration of this complexity. Similar BCAOD$_{550}$ magnitudes mask fundamentally different absorption-scattering dynamics driven by differences in BC microphysics and

625 column abundance, leading to divergent radiative outcomes and regional climate implications. These results underscore the limitations of mass-based or bulk optical approaches, including methods that infer PM$_{2.5}$ or radiative effects from AOD alone (W. Chen et al., 2020; Kang et al., 2025; Ma et al., 2022; Wei et al., 2023), which inherently overlook the microphysical processes influencing the BC absorption efficiency and mass absorption cross-section variability.

ML surrogates trained on the RTM ensemble outperforms linear and parametric approaches across a wide range of pollution

630 and microphysical regimes. Despite modest bias-variance trade-offs in transitional TOA regimes, the ML framework retains robust predictive ability. SHAP analysis further reveals that BC radiative forcing is governed by strongly non-linear interactions among BCAOD$_{550}$, mixing state, and N$_c$, with no universal threshold separating cooling and warming regimes.

Instead, a transitional regime emerges in which scattering increases more rapidly than absorption at high aerosol loading, with region-dependent moderation and overall expression. In industrial Xuzhou, enhanced scattering dominates at high loadings due to rapid aging and internal mixing with co-emitted species including sulfate and nitrate, qualitatively illustrated by the pronounced directional haze contrast in Supplement Figure S4. In contrast, in biomass-burning-dominated Dhaka, absorption remains comparatively strong owing to larger, less-coated BC cores, consistent with observations from other combustion-intensive regions (Guan et al., 2025). These findings demonstrate that no universal parameterization of BC forcing is currently feasible and that BC climate impacts are inseparable from source-specific microphysics and local environmental conditions.

Apparent transferability limitations emerge clearly in ML^{*} applications, where systematic biases reflect mismatches in underlying aerosol microphysics rather than random error. These effects are substantially mitigated in the ML^{**} model, which achieves error metrics comparable to, and in many cases lower than, region-specific ML and well below the inter-model spread reported for BCTOA DRF. As such, ML^{**} can serve as a computationally efficient surrogate to augment under well-characterized aerosol regimes, and act in-situ for repeated RTM simulations required for regional BCTOA assessment. For practical deployment, two diagnostics are essential: (i) verifying overlap between the target region and training distributions of key predictors (e.g., BC core size, mixing-state, $BCAOD_{550}$, and N_c), and (ii) confirming consistency in dominant forcing drivers using SHAP attribution. Significant divergence in either indicates reduced transferability and the continued need for RTM benchmarking.

While this framework captures key microphysical controls on BCTOA, several assumptions define its present scope. The use of a core–shell representation with a non-absorbing sulfate proxy reflects a deliberate optical constraint. Although urban aerosols arise from diverse emission sources, extensive field evidence across urban, industrial, and biomass-burning regions in East and South Asia indicates that BC is frequently internally mixed and coated by optically similar inorganic and organic material (Kompalli et al., 2021; Peng et al., 2016; Sun et al., 2024; Zamora et al., 2019), supporting the physical relevance of this assumption. However, particles with irregular shapes, including fractal aggregates, agglomerated structures are known to occur prominently in freshly emitted BC, are not explicitly addressed in this study. Future extensions could reconcile this limitation through hybrid frameworks that couple fractal or irregular morphologies at emission with spherical coated particles at advanced aging stages. Next, the treatment of organic aerosols follows an optical rather than chemical constraint, with purely scattering organic carbon treated similarly to nitrate and sulfate, while the absorption associated with absorbing organic carbon (aOC) is not explicitly prescribed but is filtered through a strict multi-band SSA consistency requirement. As described in previous studies (Liu et al., 2024b, c), the multi-waveband optical consistency inherently favours particles exhibiting stable cross-band absorption characteristic of BC, while disfavouring wavelength-confined absorbers whose absorption is confined to shorter wavelengths, such as aOC (Flores et al., 2014; Forrister et al., 2015; Lambe et al., 2013; Park et al., 2010). Additional limitations arise from the conservative spatial representativity of merged AERONET-TROPOMI SSA constraints, where pixel exclusion prioritizes physical admissibility over spatial completeness; denser ground-based networks and expanded geostationary coverage offer a pathway to relax these constraints. Finally, vertical variability of BC remains unresolved, reflecting both methodological choices and the maturity of current observing systems. Emerging multispectral GRASP-based

TROPOMI products (Chen et al., 2024; Litvinov et al., 2024), together with new global BC microphysical datasets (Liu et al., 2026), provide a direct route to extend this framework without substantially altering its core physical foundations.

670 Finally, this study computes clear-sky BCDRF at the TOA, surface, and within the atmosphere. However, the analysis presented here emphasizes BCTOA, as it isolates the net radiative perturbation directly attributable to BC. As the primary contributor to the instantaneous radiative energy imbalance caused by BC, BCTOA provides an unambiguous metric for assessing BC-specific climate forcing and feedbacks under clear-sky conditions. Follow-up work will extend this framework to jointly analyse the spatio-temporal variability of TOA, surface, and net atmospheric BC forcing components and provide a more complete assessment of BC radiative impacts over these contrasting urban regions.

675 **Appendices**

Appendix A

Mie model:

Mie theory provides a classical solution to Maxwell's equations describing the scattering of electromagnetic waves by homogeneous spherical particles, widely used to model aerosol scattering properties (Bohren and Huffman, 1998; Mie, 1908)
680 such as extinction efficiency (Q_{ext}), scattering efficiency (Q_{scat}), single scattering albedo (SSA), and asymmetry factor (g). The Mie model used in (Tiwari et al., 2023, 2025) characterizes BC aerosol particles as coated spheres, consisting of a black carbon (BC) core with sizes ranging from 50 to 500 nm and m = 2.0 + 1.0i (Schuster, 2005), coated by a non-absorbing sulfate (Sul) shell sized between 10 and 800 nm and m = 1.52–5 × 10^{-4}i (Aouizerats et al., 2010). This core-shell configuration allows us to analyze scattering properties at the single-particle level while varying particle size and mixing state, constrained qualitatively
685 by multi-waveband observational data and their uncertainties.

While the Mie model's assumption of spherical, core-shell particles does not capture the full complexity of aerosol morphology-such as agglomerated or irregularly shaped particles-numerous studies have demonstrated that this approach remains representative for BC aerosols in regions dominated by urban, industrial, and biomass burning sources, particularly across South Asia and China (Kompalli et al., 2021; Liu et al., 2020b; Peng et al., 2016; Wang et al., 2021; Zamora et al.,
690 2019). The core-shell assumption simplifies the optical modeling while effectively capturing key interactions between incident radiation and particle morphology relevant to these environments.

Tiwari et al., (2025) derived size, mixing state, column mass and number density over Xuzhou, China and Dhaka, Bangladesh using this morphological setup adopting sulfate as a proxy for the non-absorbing shell material due to its optical similarity to other common scattering aerosol coatings such as nitrate and ammonium. Literature shows that differences in extinction
695 efficiency and SSA among these species are minimal, typically within 2%, and further reduced when mixed with aerosol water (Dai et al., 2024). Another study demonstrated that ammonium sulfate's refractive index remains nearly constant under varying humidity, with negligible absorption changes (Erlick et al., 2011). Thus, categorizing sulfate, nitrate, ammonium, and similar species collectively as scattering aerosols is justified, based on their low absorption characteristics, supporting the use of sulfate

as an effective scattering shell proxy in the used core-shell model. Furthermore, the exclusion of secondary organic aerosol
(SOA) particularly absorbing organic carbon (aOC) from analysis is grounded within the methodological screening. Our
approach emphasizes identifying core-shell size combinations that exhibit absorption consistent with all observations made
across the UV, VIS, and NIR bands in tandem, a trait commonly associated with aerosols like black carbon(Bond and
Bergstrom, 2006; Samset et al., 2018a). SOA and aOC exhibit strong UV absorption but diminishing visible and near-infrared
absorption, leading to instability in SSA across wavebands and failure to meet the filtering criteria derived from observations.
Furthermore, aOC undergoes rapid photochemical bleaching and mass absorption cross-section reduction within hours to a
single diurnal cycle after emission, transitioning from absorbing to primarily scattering behavior (Forrister et al., 2015; Lambe
et al., 2013; McMeeking et al., 2011; Park et al., 2010; Saleh et al., 2013). Sensitivity tests incorporating aOC within the shell
layer of BC cores was conducted by (Liu et al., 2024b) , revealing lower aerosol absorption retrievals and reduces the number
of valid pixels raising question on the physical realism of aOC absorption in aged aerosols, particularly in urban environments
where chemical aging accelerates. Consequently, our model prioritizes particles with, cross-band absorption characteristics
consistent with BC and sulfate, effectively excluding SOA from the core-shell assumption. This method prioritizes consistency
with BC aerosol type and variable size and mixing state, potentially excluding some cases with similar loading but differing
optical characteristics. Although conservative, this exclusion enhances the reliability of the inverted results ascertaining the
pixel for BC. Future expansion of observational networks and studies will be essential to refine the selection of optimal
solutions from the probabilitic solution developed using this approach, improving the accuracy of BC concentration monitoring
in varied urban settings and deepening insight into emissions amid dynamic urban-industrial changes.

Appendix B

Satellite and Reanalysis Dataset processing for SBDART model Simulation

Multi-Angle Implementation of Atmospheric Correction (MAIAC) algorithm-based AOD

MODIS aerosol products, widely utilized for regional and global analyses (Tian et al., 2023; Wei et al., 2020), are derived
primarily from three algorithms: Dark Target (DT), Deep Blue (DB), and MAIAC (Qin et al., 2021). The DT algorithm is
limited by its limited ability to retrieve aerosol optical properties over bright surfaces such as urban areas, deserts, and the
Gobi region. The DB algorithm, meanwhile, assumes that short-wave infrared bands, that exhibit minimal reflectance influence
from vegetation (Hsu et al., 2013; Sayer et al., 2013), which can cause errors in aerosol optical depth (AOD) retrievals,
especially under polluted conditions.

The MAIAC algorithm retrieves AOD over land by applying time series analysis to distinguish aerosol signals from surface
reflectance, while explicitly accounting for the bidirectional reflectance distribution function (BRDF) of the terrain (Lyapustin
et al., 2011). By integrating temporal and spatial image processing, MAIAC effectively corrects atmospheric effects, enabling
reliable AOD retrievals even over bright surfaces and densely vegetated areas (Lyapustin et al., 2011, 2018). Compared to the
DT and DB algorithms, MAIAC offers enhanced spatial coverage with a spatial resolution of 1 km × 1 km daily data. This
study employs MCD19A2 AOD data at 470 nm and 550 nm wavelengths, accessed from the LAADS DAAC archive

(https://ladsweb.modaps.eosdis.nasa.gov/search/order/1/MCD19A2--61). To ensure data integrity, pixels were rigorously filtered following the MAIAC Collection 6.1 quality assurance protocols, including cloud masking, adjacency effect screening,

735 and AOD quality flags. Only pixels flagged as 'Clear', 'Normal Condition/Clear', and 'Best Quality with No glint' were retained for analysis. MAIAC AOD products have been extensively validated at both regional and global scales, including over South Asia, demonstrating superior accuracy compared to DT and DB algorithms (Mhawish et al., 2019). Global study has reported strong agreement with ground-based AERONET observations, with correlation coefficients exceeding 0.8 at over two-thirds of monitoring sites (Qin et al., 2021).

740 **Total Column Precipitable Water Vapor from MODIS (MYD05 and MOD05)**

This study predominantly utilizes the MODIS PWV Level 2 product MYD05_L2, with MOD05_L2 data employed as a substitute when MYD05_L2 is unavailable. The MODIS PWV is derived from the ratio of three water vapor absorbing bands (0.905 μm, 0.936 μm, and 0.930 μm) to two atmospheric window bands (0.865 μm and 1.240 μm) (King et al., 1992). While both IR and NIR channels provide PWV information, this study opts for the NIR product due to its lower sensitivity to

745 atmospheric temperature compared to atmospheric water vapor content (Bai et al., 2021; Zhou and Cheng, 2025). The NIR product offers a daily data at a spatial resolution of 1×1 km.

Given the sensitivity of MODIS PWV to cloud presence in the field of view (He and Liu, 2019), a series of rigorous quality assurance measures were implemented to retain only the most reliable pixels. The study explicitly checks for Cloud Mask QA flags, retaining only those pixels with 'Cloud Mask Status Flag' marked as 'determined' and 'Cloudiness Flag' as 'Confident

750 clear'. Furthermore, each pixel undergoes scrutiny for product quality and retrieval processing flags. Only pixels with PWV (NIR) 'Usefulness Flag' designated as 'Useful' and 'Confidence Flag' as 'Good' or 'Very Good confidence' are incorporated into the study. For a comprehensive understanding of the physical background of the retrieval method, the retrieval algorithm, adapted inversion technique, uncertainty estimates, and validation, readers are directed to the detailed study conducted by He and Liu, (2019). Since the MOD05/MYD05_L2 data only has geolocation scientific data set for PWV(IR) at 5×5 km, this

755 study separately downloaded MYD03_L2/MOD03_L2 1km Geolocation data and collocated MYD05 and MYD03. Both MOD/MYD03_L2 and MOD/MYD05_L2 datasets utilized in this study are publicly accessible via the NASA's Level-1 and Atmosphere Archive & Distribution System Distributed Active Archive Center (LAADS DAAC) (URL: https://ladsweb.modaps.eosdis.nasa.gov/search/order/2/MYD03--61,MYD05_L2--61).

Surface Spectral Albedo from MODIS BRDF Albedo model (MCD43A1)

760 In this study, we utilize the MCD43A1 dataset, which includes MODIS, Terra and Aqua BRDF/Albedo model parameters on a daily basis at a 500m resolution, to compute the actual blue-sky albedo. This measured albedo is employed in the radiative transfer model as the surface albedo, replacing the predefined values used by the model.

The MODIS BRDF/albedo algorithm, based on the three-parameter Ross-Thick-Li-Sparse-Reciprocal model, estimates kernel parameters from clear-sky surface reflectance collected by Terra and Aqua MODIS sensors(Lucht et al., 2000; Román et al.,

765 2010; Schaaf et al., 2002). These parameters include the isotropic parameter (f_{iso}), the kernel for volume scattering (K_{vol}), and the kernel derived from surface scattering and geometric shadow theory (K_{geo}). They are available for each MODIS spectral

band and for three broad bands: 0.3–0.7 µm, 0.7–5.0 µm, and 0.3–5.0 µm. These parameters can be utilized in the forward model to reconstruct surface anisotropic effects, allowing for the correction of directional reflectance. From the MCD43A1.061 files, layers of BRDF Albedo Parameters for visible, near infrared and shortwave bands along with their respective albedo

770 band mandatory quality flags are used. The weighting parameters described above are used to compute integrated directional hemispherical reflectance also known as Black-sky Albedo (albedo in the absence of a diffuse component and is a function of solar zenith angle) at local solar zenith angle, and bihemispherical reflectance or White-sky albedo (albedo measured without direct sunlight when the diffuse component is isotropic). Together, these two types of albedos represent the extremes of completely direct and completely diffuse illumination. Finally, the actual blue-sky albedo is derived as an interpolated value

775 between these extremes (Jia et al., 2022), depending upon the fraction of diffuse skylight present. This fraction, itself a function of the aerosol optical depth (Giannaklis et al., 2023). For each short-wave, visible and near-infrared band, we compute the actual blue-sky albedo using the above method and finally spectral average of the blue-sky albedo is taken across these wavebands which serves as the input for radiative transfer model (RTM). This approach aligns with previous methods, where surface albedo values are averaged across the four operational AERONET wavebands. This spectral averaging has been

780 demonstrated to provide a reliable approximation for estimating direct aerosol radiative forcing at the surface (García et al., 2012; Logothetis et al., 2021).

The fundamental equations for calculating black-sky and white-sky albedo using the BRDF kernels, as well as the global assessment/validation of these albedo products, have been extensively covered in earlier literature assuring the quality of the product (Che et al., 2017; Wang et al., 2015). NASA's Application for Extracting and Exploring Analysis Ready Samples

785 (AppEEARS) platform, offers efficient tool for extracting the required layers of data for desired temporal and spatial range. The MCD43A1.061 data can be sourced from https://appeears.earthdatacloud.nasa.gov/task/area.

Total Column Ozone from Sentinel-5P TROPOMI (TROPOspheric Monitoring Instrument)

The total column ozone data used in this study were obtained from the Sentinel-5P TROPOMI (TROPOspheric Monitoring Instrument) S5P_L2__O3_TOT_HiR product, which provides data at a high spatial resolution of 5.5 × 3.5 km (Inness et al.,

790 2019; Sullivan et al., 2022). This study uses dataset derived from offline and reprocessed products, which employs the GOME-type Direct FITting (GODFIT) algorithm. This advanced retrieval algorithm enhances the accuracy of total ozone measurements by directly fitting simulated radiances in the Huggins bands (325–335nm) to observational data (Garane et al., 2019). The adjustment process involves varying key atmospheric parameters, including total ozone concentration, effective scene albedo, and effective temperature. To retain only the best pixel, for total column ozone, the study implements a pixel-

795 by-pixel data quality assurance assuring that qa_value is greater than 0.5 following the recommendation of S5P Mission Performance Centre OFFL/RPRO Total ozone Readme Manual.

The   S5P_L2__O3_TOT_HiR   can   be   sourced   from: https://disc.gsfc.nasa.gov/datasets/S5P_L2__O3_TOT_HiR_2/summary?keywords=Total%20column%20ozone. This study used the spatio-temporal data subsetting tool provided by Goddard Earth Sciences Data and Information Services Centre (GES

800 DISC) to source the data for desired spatio-temporal range. A comprehensive validation of this product, using both global

ground-based and contemporary satellite observations, was conducted by Garane et al., (2019). In a more recent study, various factors–such as solar zenith angle, surface albedo, and measurement parameters like scan angle–and their impact on the uncertainty in TROPOMI's ozone profile retrievals were investigated (Keppens et al., 2024).

Data and Code availability

805   The level-2 raw satellite datasets for different products used in this study were downloaded from publicly accessible NASA data archives.

TROPOMAER SSA products are available from the NASA GES DISC (https://disc.gsfc.nasa.gov/datasets/TROPOMAER_1/summary?keywords=TROPOMAER). MAIAC MCD19A2 AOD data can be downloaded from the NASA LAADS DAAC (https://ladsweb.modaps.eosdis.nasa.gov/search/order/1/MCD19A2--61).

810   MODIS geolocation datasets (MOD03_L2/MYD03_L2) and collocated water vapor products (MOD05_L2/MYD05_L2) are available through LAADS DAAC (https://ladsweb.modaps.eosdis.nasa.gov/search/order/2/MYD03--61,MYD05_L2--61) Surface spectral albedo from the MODIS BRDF–Albedo model (MCD43A1.061) was obtained from NASA AppEEARS (https://appeears.earthdatacloud.nasa.gov/task/area), and total column ozone data from the Sentinel-5P TROPOMI S5P_L2__O3_TOT_HiR product were accessed via NASA GES DISC

815   (https://disc.gsfc.nasa.gov/datasets/S5P_L2__O3_TOT_HiR_2/summary?keywords=Total%20column%20ozone). One can download these products for specified time ranges and spatial domains encompassing Xuzhou and Dhaka.

The radiative-transfer calculations employed the SBDART model sourced from https://github.com/paulricchiazzi/SBDART. The COSMO model used the baseline Mie model (later author modified for SSA constraint) from https://github.com/garatbeo/Mie-Simulation-Maetzler-MATLAB-code/blob/main/maetzler_mie_v2.pdf.

820   All processed datasets and code supporting this study are archived in Figshare data repository link provided for peer review: https://figshare.com/s/683ebfd680d1ede7698f. Due to their large size data have been compressed for storage. Each folder can be extracted individually which contains sequential steps, from using microphysical BC data from Tiwari et al., (2025), processing ancillary satellite inputs, example codes of Mie and radiative-transfer modules, as well as the surrogate machine-learning models.

825   **Author contributions**

P.T. conceptualized the study, curated the data, developed the methodological framework, performed the formal analysis and investigation, created the visualizations, and prepared the original manuscript draft, with subsequent revisions. **J.B.C.** supervised the research, validated the results, and contributed to the writing, review, and editing of the manuscript. **H.G.** contributed to data curation and investigation. **L.L.** contributed to the investigation and manuscript review and editing. **J.W.**

830   and **O.D.** contributed to validation and manuscript review and editing. **K.Q.** supervised the project and validated the results.

Competing interests

The authors have the following competing interests: One of the authors is a member of the editorial board of ACP.

Acknowledgements

Financial support

References

Aouizerats, B., Thouron, O., Tulet, P., Mallet, M., Gomes, L., and Henzing, J. S.: Development of an online radiative module
for the computation of aerosol optical properties in 3-D atmospheric models: validation during the EUCAARI campaign,
845   Geosci Model Dev, 3, 553–564, https://doi.org/10.5194/gmd-3-553-2010, 2010.
Bai, J., Lou, Y., Zhang, W., Zhou, Y., Zhang, Z., and Shi, C.: Assessment and calibration of MODIS precipitable water vapor
products based on GPS network over China, Atmos Res, 254, 105504, https://doi.org/10.1016/j.atmosres.2021.105504, 2021.
Bellouin, N., Boucher, O., Haywood, J., and Reddy, M. S.: Global estimate of aerosol direct radiative forcing from satellite
measurements, Nature, 438, 1138–1141, https://doi.org/10.1038/nature04348, 2005.
850   Bohren, C. F. and Huffman, D. R.: Absorption and Scattering of Light by Small Particles, Wiley,
https://doi.org/10.1002/9783527618156, 1998.
Bond, T. C. and Bergstrom, R. W.: Light Absorption by Carbonaceous Particles: An Investigative Review, Aerosol Science
and Technology, 40, 27–67, https://doi.org/10.1080/02786820500421521, 2006.
Bond, T. C., Doherty, S. J., Fahey, D. W., Forster, P. M., Berntsen, T., Deangelo, B. J., Flanner, M. G., Ghan, S., Kärcher, B.,
855   Koch, D., Kinne, S., Kondo, Y., Quinn, P. K., Sarofim, M. C., Schultz, M. G., Schulz, M., Venkataraman, C., Zhang, H.,
Zhang, S., Bellouin, N., Guttikunda, S. K., Hopke, P. K., Jacobson, M. Z., Kaiser, J. W., Klimont, Z., Lohmann, U., Schwarz,
J. P., Shindell, D., Storelvmo, T., Warren, S. G., and Zender, C. S.: Bounding the role of black carbon in the climate system:

A scientific assessment, Journal of Geophysical Research Atmospheres, 118, 5380–5552, https://doi.org/10.1002/jgrd.50171, 2013.

860 Cappa, C. D., Onasch, T. B., Massoli, P., Worsnop, D. R., Bates, T. S., Cross, E. S., Davidovits, P., Hakala, J., Hayden, K. L., Jobson, B. T., Kolesar, K. R., Lack, D. A., Lerner, B. M., Li, S.-M., Mellon, D., Nuaaman, I., Olfert, J. S., Petäjä, T., Quinn, P. K., Song, C., Subramanian, R., Williams, E. J., and Zaveri, R. A.: Radiative Absorption Enhancements Due to the Mixing State of Atmospheric Black Carbon, Science (1979), 337, 1078–1081, https://doi.org/10.1126/science.1223447, 2012.

Che, X., Feng, M., Sexton, J., Channan, S., Yang, Y., and Sun, Q.: Assessment of MODIS BRDF/Albedo Model Parameters 865 (MCD43A1 Collection 6) for Directional Reflectance Retrieval, Remote Sens (Basel), 9, 1123, https://doi.org/10.3390/rs9111123, 2017.

Chen, C., Dubovik, O., Schuster, G. L., Chin, M., Henze, D. K., Lapyonok, T., Li, Z., Derimian, Y., and Zhang, Y.: Multi-angular polarimetric remote sensing to pinpoint global aerosol absorption and direct radiative forcing, Nat Commun, 13, 7459, https://doi.org/10.1038/s41467-022-35147-y, 2022.

870 Chen, C., Litvinov, P., Dubovik, O., Bindreiter, L., Matar, C., Fuertes, D., Lopatin, A., Lapyonok, T., Lanzinger, V., Hangler, A., Aspetsberger, M., de Graaf, M., Tilstra, L. G., Stammes, P., Dandocsi, A., Gasbarra, D., Fluck, E., Zehner, C., and Retscher, C.: Extended aerosol and surface characterization from S5P/TROPOMI with GRASP algorithm. Part II: Global validation and Intercomparison, Remote Sens Environ, 313, 114374, https://doi.org/10.1016/j.rse.2024.114374, 2024.

Chen, G., Wang, J., Wang, Y., Wang, J., Jin, Y., Cheng, Y., Yin, Y., Liao, H., Ding, A., Wang, S., Hao, J., and Liu, C.: An 875 Aerosol Optical Module With Observation-Constrained Black Carbon Properties for Global Climate Models, J Adv Model Earth Syst, 15, https://doi.org/10.1029/2022MS003501, 2023.

Chen, W., Tian, H., and Qin, K.: Black Carbon Aerosol in the Industrial City of Xuzhou, China: Temporal Characteristics and Source Appointment, Aerosol Air Qual Res, 19, 794–811, https://doi.org/10.4209/aaqr.2018.07.0245, 2019.

Chen, W., Ran, H., Cao, X., Wang, J., Teng, D., Chen, J., and Zheng, X.: Estimating PM2.5 with high-resolution 1-km AOD 880 data and an improved machine learning model over Shenzhen, China, Science of The Total Environment, 746, 141093, https://doi.org/10.1016/j.scitotenv.2020.141093, 2020.

Chin, M., Ginoux, P., Kinne, S., Torres, O., Holben, B. N., Duncan, B. N., Martin, R. V., Logan, J. A., Higurashi, A., and Nakajima, T.: Tropospheric Aerosol Optical Thickness from the GOCART Model and Comparisons with Satellite and Sun Photometer Measurements, J Atmos Sci, 59, 461–483, https://doi.org/10.1175/1520-0469(2002)059, 2002.

885 Chung, C. E.: Aerosol Direct Radiative Forcing: A Review, in: Atmospheric Aerosols - Regional Characteristics - Chemistry and Physics, InTech, https://doi.org/10.5772/50248, 2012.

Cohen, J. B. and Prinn, R. G.: Development of a fast, urban chemistry metamodel for inclusion in global models, Atmos Chem Phys, 11, 7629–7656, https://doi.org/10.5194/acp-11-7629-2011, 2011.

Cohen, J. B. and Wang, C.: Estimating global black carbon emissions using a top-down Kalman Filter approach, Journal of 890 Geophysical Research: Atmospheres, 119, 307–323, https://doi.org/https://doi.org/10.1002/2013JD019912, 2014.

Colin, B., Schmidt, M., Clifford, S., Woodley, A., and Mengersen, K.: Influence of Spatial Aggregation on Prediction Accuracy of Green Vegetation Using Boosted Regression Trees, Remote Sens (Basel), 10, 1260, https://doi.org/10.3390/rs10081260, 2018.

Dai, C., Zhang, X., Lian, W., Wei, H., Liu, J., and Zou, S.: Comparison study between nitrate and sulfate aerosols and their

895   coating effect on the scattering properties of mineral aerosol, Sci Rep, 14, 21756, https://doi.org/10.1038/s41598-024-71532-x, 2024.

Dasari, S., Andersson, A., Stohl, A., Evangeliou, N., Bikkina, S., Holmstrand, H., Budhavant, K., Salam, A., and Gustafsson, Ö.: Source Quantification of South Asian Black Carbon Aerosols with Isotopes and Modeling, Environ Sci Technol, 54, 11771–11779, https://doi.org/10.1021/acs.est.0c02193, 2020.

900   Ding, S. and Liu, D.: Evaluation of the CAMS reanalysis for atmospheric black carbon and carbon monoxide over the north China plain, Environmental Pollution, 314, 120286, https://doi.org/10.1016/j.envpol.2022.120286, 2022.

Erlick, C., Abbatt, J. P. D., and Rudich, Y.: How Different Calculations of the Refractive Index Affect Estimates of the Radiative Forcing Efficiency of Ammonium Sulfate Aerosols, J Atmos Sci, 68, 1845–1852, https://doi.org/10.1175/2011JAS3721.1, 2011.

905   Everett, J. T., Newton, E. N., and Odum, M. M.: A Review of Progress in Constraining Global Black Carbon Climate Effects, Earth Systems and Environment, 6, 771–785, https://doi.org/10.1007/s41748-022-00313-1, 2022.

Fernandes, A., Szkop, A., and Pietruczuk, A.: Comparison of the Performance of the GRASP and MERRA2 Models in Reproducing Tropospheric Aerosol Layers, Atmosphere (Basel), 14, 1409, https://doi.org/10.3390/atmos14091409, 2023.

Fierce, L., Onasch, T. B., Cappa, C. D., Mazzoleni, C., China, S., Bhandari, J., Davidovits, P., Fischer, D. Al, Helgestad, T.,

910   Lambe, A. T., Sedlacek, A. J., Smith, G. D., and Wolff, L.: Radiative absorption enhancements by black carbon controlled by particle-to-particle heterogeneity in composition, Proceedings of the National Academy of Sciences, 117, 5196–5203, https://doi.org/10.1073/pnas.1919723117, 2020.

Flores, J. M., Zhao, D. F., Segev, L., Schlag, P., Kiendler-Scharr, A., Fuchs, H., Watne, Å. K., Bluvshtein, N., Mentel, Th. F., Hallquist, M., and Rudich, Y.: Evolution of the complex refractive index in the UV spectral region in ageing secondary organic

915   aerosol, Atmos Chem Phys, 14, 5793–5806, https://doi.org/10.5194/acp-14-5793-2014, 2014.

Forrister, H., Liu, J., Scheuer, E., Dibb, J., Ziemba, L., Thornhill, K. L., Anderson, B., Diskin, G., Perring, A. E., Schwarz, J. P., Campuzano-Jost, P., Day, D. A., Palm, B. B., Jimenez, J. L., Nenes, A., and Weber, R. J.: Evolution of brown carbon in wildfire plumes, Geophys Res Lett, 42, 4623–4630, https://doi.org/10.1002/2015GL063897, 2015.

Forster, P. M., Smith, C. J., Walsh, T., Lamb, W. F., Lamboll, R., Hauser, M., Ribes, A., Rosen, D., Gillett, N., Palmer, M.

920   D., Rogelj, J., von Schuckmann, K., Seneviratne, S. I., Trewin, B., Zhang, X., Allen, M., Andrew, R., Birt, A., Borger, A., Boyer, T., Broersma, J. A., Cheng, L., Dentener, F., Friedlingstein, P., Gutiérrez, J. M., Gütschow, J., Hall, B., Ishii, M., Jenkins, S., Lan, X., Lee, J.-Y., Morice, C., Kadow, C., Kennedy, J., Killick, R., Minx, J. C., Naik, V., Peters, G. P., Pirani, A., Pongratz, J., Schleussner, C.-F., Szopa, S., Thorne, P., Rohde, R., Rojas Corradi, M., Schumacher, D., Vose, R., Zickfeld, K., Masson-Delmotte, V., and Zhai, P.: Indicators of Global Climate Change 2022: annual update of large-scale indicators of

925   the state of the climate system and human influence, Earth Syst Sci Data, 15, 2295–2327, https://doi.org/10.5194/essd-15-2295-2023, 2023.

Garane, K., Koukouli, M.-E., Verhoelst, T., Lerot, C., Heue, K.-P., Fioletov, V., Balis, D., Bais, A., Bazureau, A., Dehn, A., Goutail, F., Granville, J., Griffin, D., Hubert, D., Keppens, A., Lambert, J.-C., Loyola, D., McLinden, C., Pazmino, A., Pommereau, J.-P., Redondas, A., Romahn, F., Valks, P., Van Roozendael, M., Xu, J., Zehner, C., Zerefos, C., and Zimmer,

930   W.: TROPOMI/S5P total ozone column data: global ground-based validation and consistency with other satellite missions, Atmos Meas Tech, 12, 5263–5287, https://doi.org/10.5194/amt-12-5263-2019, 2019.

García, O. E., Díaz, J. P., Expósito, F. J., Díaz, A. M., Dubovik, O., Derimian, Y., Dubuisson, P., and Roger, J.-C.: Shortwave radiative forcing and efficiency of key aerosol types using AERONET data, Atmos Chem Phys, 12, 5129–5145, https://doi.org/10.5194/acp-12-5129-2012, 2012.

935   Gautam, R., Patel, P. N., Singh, M. K., Liu, T., Mickley, L. J., Jethva, H., and DeFries, R. S.: Extreme Smog Challenge of India Intensified by Increasing Lower Tropospheric Stability, Geophys Res Lett, 50, https://doi.org/10.1029/2023GL103105, 2023.

Giannaklis, C.-P., Logothetis, S.-A., Salamalikis, V., Tzoumanikas, P., Katsidimas, K., and Kazantzidis, A.: Simulations of Sky Radiances in Red and Blue Channels at Various Aerosol Conditions Using Radiative Transfer Modeling, in: 16th

940   International Conference on Meteorology, Climatology and Atmospheric Physics—COMECAP 2023, 89, https://doi.org/10.3390/environsciproc2023026089, 2023.

de Graaf, Martin.: TROPOMI validation report of the Aerosol Optical Thickness product, Netherlands, 13 pp., 2022.

Guan, L., Cohen, J. B., Wang, S., Tiwari, P., Liu, Z., and Qin, K.: In-Tandem Multi-Waveband Particulate Absorption and Size Observations Yield Substantial Increase in Radiative Forcing over Industrial Central China, EGUsphere [preprint],

945   https://doi.org/10.5194/egusphere-2025-3229, 2025.

Hansen, J. E. and Sato, M.: Trends of measured climate forcing agents, Proceedings of the National Academy of Sciences, 98, 14778–14783, https://doi.org/10.1073/pnas.261553698, 2001.

He, J. and Liu, Z.: Comparison of Satellite-Derived Precipitable Water Vapor Through Near-Infrared Remote Sensing Channels, IEEE Transactions on Geoscience and Remote Sensing, 57, 10252–10262,

950   https://doi.org/10.1109/TGRS.2019.2932847, 2019.

Hsu, N. C., Jeong, M. J., Bettenhausen, C., Sayer, A. M., Hansell, R., Seftor, C. S., Huang, J., and Tsay, S. C.: Enhanced Deep Blue aerosol retrieval algorithm: The second generation, Journal of Geophysical Research Atmospheres, 118, 9296–9315, https://doi.org/10.1002/jgrd.50712, 2013.

Inness, A., Flemming, J., Heue, K.-P., Lerot, C., Loyola, D., Ribas, R., Valks, P., van Roozendael, M., Xu, J., and Zimmer,

955   W.: Monitoring and assimilation tests with TROPOMI data in the CAMS system: near-real-time total column ozone, Atmos Chem Phys, 19, 3939–3962, https://doi.org/10.5194/acp-19-3939-2019, 2019.

Jacobson, M. Z.: Strong radiative heating due to the mixing state of black carbon in atmospheric aerosols, Nature, 409, 695–697, https://doi.org/10.1038/35055518, 2001.

Jia, A., Wang, D., Liang, S., Peng, J., and Yu, Y.: Global Daily Actual and Snow-Free Blue-Sky Land Surface Albedo
960 Climatology From 20-Year MODIS Products, Journal of Geophysical Research: Atmospheres, 127,
https://doi.org/10.1029/2021JD035987, 2022.

Kahn, R. A., Andrews, E., Brock, C. A., Chin, M., Feingold, G., Gettelman, A., Levy, R. C., Murphy, D. M., Nenes, A., Pierce,
J. R., Popp, T., Redemann, J., Sayer, A. M., da Silva, A. M., Sogacheva, L., and Stier, P.: Reducing Aerosol Forcing
Uncertainty by Combining Models With Satellite and Within-The-Atmosphere Observations: A Three-Way Street, Reviews
965 of Geophysics, 61, https://doi.org/10.1029/2022RG000796, 2023.

Kang, J., Wang, S., Cohen, J., Wang, W., Shi, L., Wang, T., Sun, Q., Feng, J., and Qin, K.: Improving estimation of surface
PM 2.5 by including satellite observations of gases, aerosols, and radiation in tandem, Environmental Research Letters, 20,
124019, https://doi.org/10.1088/1748-9326/ae1e17, 2025.

Kelesidis, G. A., Neubauer, D., Fan, L.-S., Lohmann, U., and Pratsinis, S. E.: Enhanced Light Absorption and Radiative
970 Forcing by Black Carbon Agglomerates, Environ Sci Technol, 56, 8610–8618, https://doi.org/10.1021/acs.est.2c00428, 2022.

Keppens, A., Di Pede, S., Hubert, D., Lambert, J.-C., Veefkind, P., Sneep, M., De Haan, J., ter Linden, M., Leblanc, T.,
Compernolle, S., Verhoelst, T., Granville, J., Nath, O., Fjæraa, A. M., Boyd, I., Niemeijer, S., Van Malderen, R., Smit, H. G.
J., Duflot, V., Godin-Beekmann, S., Johnson, B. J., Steinbrecht, W., Tarasick, D. W., Kollonige, D. E., Stauffer, R. M.,
Thompson, A. M., Dehn, A., and Zehner, C.: 5 years of Sentinel-5P TROPOMI operational ozone profiling and geophysical
975 validation using ozonesonde and lidar ground-based networks, Atmos Meas Tech, 17, 3969–3993, https://doi.org/10.5194/amt-
17-3969-2024, 2024.

King, M. D., Kaufman, Y. J., Menzel, W. P., and Tanre, D.: Remote sensing of cloud, aerosol, and water vapor properties from
the moderate resolution imaging spectrometer (MODIS), IEEE Transactions on Geoscience and Remote Sensing, 30, 2–27,
https://doi.org/10.1109/36.124212, 1992.

980 Koch, D. and Del Genio, A. D.: Black carbon semi-direct effects on cloud cover: review and synthesis, Atmos Chem Phys,
10, 7685–7696, https://doi.org/10.5194/acp-10-7685-2010, 2010.

Kompalli, S. K., Babu, S. N. S., Moorthy, K. K., Satheesh, S. K., Gogoi, M. M., Nair, V. S., Jayachandran, V. N., Liu, D.,
Flynn, M. J., and Coe, H.: Mixing state of refractory black carbon aerosol in the South Asian outflow over the northern Indian
Ocean during winter, Atmos Chem Phys, 21, 9173–9199, https://doi.org/10.5194/acp-21-9173-2021, 2021.

985 Lambe, A. T., Cappa, C. D., Massoli, P., Onasch, T. B., Forestieri, S. D., Martin, A. T., Cummings, M. J., Croasdale, D. R.,
Brune, W. H., Worsnop, D. R., and Davidovits, P.: Relationship between Oxidation Level and Optical Properties of Secondary
Organic Aerosol, Environ Sci Technol, 47, 6349–6357, https://doi.org/10.1021/es401043j, 2013.

Li, J., Carlson, B. E., Yung, Y. L., Lv, D., Hansen, J., Penner, J. E., Liao, H., Ramaswamy, V., Kahn, R. A., Zhang, P.,
Dubovik, O., Ding, A., Lacis, A. A., Zhang, L., and Dong, Y.: Scattering and absorbing aerosols in the climate system, Nat
990 Rev Earth Environ, 3, 363–379, https://doi.org/10.1038/s43017-022-00296-7, 2022.

Li, W., Wang, Y., Yi, Z., Guo, B., Chen, W., Che, H., and Zhang, X.: Evaluation of MERRA-2 and CAMS reanalysis for black
carbon aerosol in China, Environmental Pollution, 343, 123182, https://doi.org/10.1016/j.envpol.2023.123182, 2024.

Litvinov, P., Chen, C., Dubovik, O., Bindreiter, L., Matar, C., Fuertes, D., Lopatin, A., Lapyonok, T., Lanzinger, V., Hangler, A., Aspetsberger, M., de Graaf, M., Tilstra, L. G., Stammes, P., Dandocsi, A., Gasbarra, D., Fluck, E., Zehner, C., and Retscher, C.: Extended aerosol and surface characterization from S5P/TROPOMI with GRASP algorithm. Part I: Conditions, approaches, performance and new possibilities, Remote Sens Environ, 313, 114355, https://doi.org/10.1016/j.rse.2024.114355, 2024.

Liu, D., Whitehead, J., Alfarra, M. R., Reyes-Villegas, E., Spracklen, D. V., Reddington, C. L., Kong, S., Williams, P. I., Ting, Y.-C., Haslett, S., Taylor, J. W., Flynn, M. J., Morgan, W. T., McFiggans, G., Coe, H., and Allan, J. D.: Black-carbon absorption enhancement in the atmosphere determined by particle mixing state, Nat Geosci, 10, 184–188, https://doi.org/10.1038/ngeo2901, 2017.

Liu, F., Yon, J., Fuentes, A., Lobo, P., Smallwood, G. J., and Corbin, J. C.: Review of recent literature on the light absorption properties of black carbon: Refractive index, mass absorption cross section, and absorption function, Aerosol Science and Technology, 54, 33–51, https://doi.org/10.1080/02786826.2019.1676878, 2020a.

Liu, H., Pan, X., Liu, D., Liu, X., Chen, X., Tian, Y., Sun, Y., Fu, P., and Wang, Z.: Mixing characteristics of refractory black carbon aerosols at an urban site in Beijing, Atmos Chem Phys, 20, 5771–5785, https://doi.org/10.5194/acp-20-5771-2020, 2020b.

Liu, J., Cohen, J. B., He, Q., Tiwari, P., and Qin, K.: Accounting for NOx emissions from biomass burning and urbanization doubles existing inventories over South, Southeast and East Asia, Commun Earth Environ, 5, 255, https://doi.org/10.1038/s43247-024-01424-5, 2024a.

Liu, J., Cohen, J. B., Tiwari, P., Liu, Z., Yim, S. H.-L., Gupta, P., and Qin, K.: New top-down estimation of daily mass and number column density of black carbon driven by OMI and AERONET observations, Remote Sens Environ, 315, 114436, https://doi.org/10.1016/j.rse.2024.114436, 2024b.

Liu, Z., Cohen, J. B., Wang, S., Wang, X., Tiwari, P., and Qin, K.: Remotely sensed BC columns over rapidly changing Western China show significant decreases in mass and inconsistent changes in number, size, and mixing properties due to policy actions, NPJ Clim Atmos Sci, 7, 124, https://doi.org/10.1038/s41612-024-00663-9, 2024c.

Liu, Z., Cohen, J. B., Tiwari, P., Guan, L., Wang, S., Li, Z., and Qin, K.: A global black carbon dataset of column concentration and microphysical information derived from MISR multi-band observations and Mie scattering simulations, Earth Syst Sci Data, 18, 507–533, https://doi.org/10.5194/essd-18-507-2026, 2026.

Loeb, N. G., Su, W., Bellouin, N., and Ming, Y.: Changes in Clear-Sky Shortwave Aerosol Direct Radiative Effects Since 2002, Journal of Geophysical Research: Atmospheres, 126, https://doi.org/10.1029/2020JD034090, 2021.

Logothetis, S.-A., Salamalikis, V., and Kazantzidis, A.: The impact of different aerosol properties and types on direct aerosol radiative forcing and efficiency using AERONET version 3, Atmos Res, 250, 105343, https://doi.org/10.1016/j.atmosres.2020.105343, 2021.

Lohmann, U. and Feichter, J.: Global indirect aerosol effects: A review, Atmos Chem Phys, 5, 715–737, https://doi.org/10.5194/ACP-5-715-2005, 2005.

Lucht, W., Schaaf, C. B., and Strahler, A. H.: An algorithm for the retrieval of albedo from space using semiempirical BRDF models, IEEE Transactions on Geoscience and Remote Sensing, 38, 977–998, https://doi.org/10.1109/36.841980, 2000.

Lundberg, S. M. and Lee, S.-I.: A Unified Approach to Interpreting Model Predictions, in: Neural Information Processing Systems, 2017.

1030

Luo, J., Li, Z., Zhang, C., Zhang, Q., Zhang, Y., Zhang, Y., Curci, G., and Chakrabarty, R. K.: Regional impacts of black carbon morphologies on shortwave aerosol–radiation interactions: a comparative study between the US and China, Atmos Chem Phys, 22, 7647–7666, https://doi.org/10.5194/acp-22-7647-2022, 2022.

Lyapustin, A. and Wang, Y.: MODIS Multi-Angle Implementation of Atmospheric Correction (MAIAC) Data User's Guide, Collection 6.1, Version 3.1, https://lpdaac.usgs.gov/documents/1500/MCD19_User_Guide_V61.pdf, November 2022.

1035

Lyapustin, A., Wang, Y., Laszlo, I., Kahn, R., Korkin, S., Remer, L., Levy, R., and Reid, J. S.: Multiangle implementation of atmospheric correction (MAIAC): 2. Aerosol algorithm, J Geophys Res, 116, D03211, https://doi.org/10.1029/2010JD014986, 2011.

Lyapustin, A., Wang, Y., Korkin, S., and Huang, D.: MODIS Collection 6 MAIAC algorithm, Atmos Meas Tech, 11, 5741–5765, https://doi.org/10.5194/amt-11-5741-2018, 2018.

1040

Ma, Z., Dey, S., Christopher, S., Liu, R., Bi, J., Balyan, P., and Liu, Y.: A review of statistical methods used for developing large-scale and long-term PM2.5 models from satellite data, Remote Sens Environ, 269, 112827, https://doi.org/10.1016/j.rse.2021.112827, 2022.

Mahajan, S., Evans, K. J., Hack, J. J., and Truesdale, J. E.: Linearity of Climate Response to Increases in Black Carbon Aerosols, J Clim, 26, 8223–8237, https://doi.org/10.1175/JCLI-D-12-00715.1, 2013.

1045

Martins, V. S., Lyapustin, A., de Carvalho, L. A. S., Barbosa, C. C. F., and Novo, E. M. L. M.: Validation of high-resolution MAIAC aerosol product over South America, Journal of Geophysical Research: Atmospheres, 122, 7537–7559, https://doi.org/10.1002/2016JD026301, 2017.

Matus, A. V., L'Ecuyer, T. S., and Henderson, D. S.: New Estimates of Aerosol Direct Radiative Effects and Forcing From A-Train Satellite Observations, Geophys Res Lett, 46, 8338–8346, https://doi.org/10.1029/2019GL083656, 2019.

1050

McFiggans, G., Artaxo, P., Baltensperger, U., Coe, H., Facchini, M. C., Feingold, G., Fuzzi, S., Gysel, M., Laaksonen, A., Lohmann, U., Mentel, T. F., Murphy, D. M., O'Dowd, C. D., Snider, J. R., and Weingartner, E.: The effect of physical and chemical aerosol properties on warm cloud droplet activation, Atmos Chem Phys, 6, 2593–2649, https://doi.org/10.5194/acp-6-2593-2006, 2006.

1055

McMeeking, G. R., Morgan, W. T., Flynn, M., Highwood, E. J., Turnbull, K., Haywood, J., and Coe, H.: Black carbon aerosol mixing state, organic aerosols and aerosol optical properties over the United Kingdom, Atmos Chem Phys, 11, 9037–9052, https://doi.org/10.5194/acp-11-9037-2011, 2011.

Mehrotra, B. J., Srivastava, A. K., Singh, A., Parashar, D., Majumder, N., Singh, R. S., Choudhary, A., and Srivastava, M. K.: Long-Term Trend in Black Carbon Mass Concentration Over Central Indo-Gangetic Plain Location: Understanding the

1060   Implied Change in Radiative Forcing, Journal of Geophysical Research: Atmospheres, 129, https://doi.org/10.1029/2024JD040754, 2024.

Mehrotra, B. J., Choudhary, A., Srivastava, A. K., Sharma, S. K., and Srivastava, M. K.: Physical, optical and radiative attributes of atmospheric aerosols produced due to bonfire during the Holika festival, Physics and Chemistry of the Earth, Parts A/B/C, 138, 103856, https://doi.org/10.1016/j.pce.2025.103856, 2025.

1065   Mhawish, A., Banerjee, T., Sorek-Hamer, M., Lyapustin, A., Broday, D. M., and Chatfield, R.: Comparison and evaluation of MODIS Multi-angle Implementation of Atmospheric Correction (MAIAC) aerosol product over South Asia, Remote Sens Environ, 224, 12–28, https://doi.org/10.1016/j.rse.2019.01.033, 2019.

Mie, G.: Beiträge zur Optik trüber Medien, speziell kolloidaler Metallösungen, Ann Phys, 330, 377–445, https://doi.org/10.1002/andp.19083300302, 1908.

1070   Myhre, G., Samset, B. H., Schulz, M., Balkanski, Y., Bauer, S., Berntsen, T. K., Bian, H., Bellouin, N., Chin, M., Diehl, T., Easter, R. C., Feichter, J., Ghan, S. J., Hauglustaine, D., Iversen, T., Kinne, S., Kirkevåg, A., Lamarque, J.-F., Lin, G., Liu, X., Lund, M. T., Luo, G., Ma, X., van Noije, T., Penner, J. E., Rasch, P. J., Ruiz, A., Seland, Ø., Skeie, R. B., Stier, P., Takemura, T., Tsigaridis, K., Wang, P., Wang, Z., Xu, L., Yu, H., Yu, F., Yoon, J.-H., Zhang, K., Zhang, H., and Zhou, C.: Radiative forcing of the direct aerosol effect from AeroCom Phase II simulations, Atmos Chem Phys, 13, 1853–1877,
1075   https://doi.org/10.5194/acp-13-1853-2013, 2013.

Nenes, A., Conant, W. C., and Seinfeld, J. H.: Black carbon radiative heating effects on cloud microphysics and implications for the aerosol indirect effect 2. Cloud microphysics, Journal of Geophysical Research: Atmospheres, 107, https://doi.org/10.1029/2002JD002101, 2002.

Park, R. J., Kim, M. J., Jeong, J. I., Youn, D., and Kim, S.: A contribution of brown carbon aerosol to the aerosol light
1080   absorption and its radiative forcing in East Asia, Atmos Environ, 44, 1414–1421, https://doi.org/10.1016/j.atmosenv.2010.01.042, 2010.

Peng, J., Hu, M., Guo, S., Du, Z., Zheng, J., Shang, D., Levy Zamora, M., Zeng, L., Shao, M., Wu, Y.-S., Zheng, J., Wang, Y., Glen, C. R., Collins, D. R., Molina, M. J., and Zhang, R.: Markedly enhanced absorption and direct radiative forcing of black carbon under polluted urban environments, Proceedings of the National Academy of Sciences, 113, 4266–4271,
1085   https://doi.org/10.1073/pnas.1602310113, 2016.

Qin, K., He, Q., Zhang, Y., Cohen, J. B., Tiwari, P., and Lolli, S.: Aloft Transport of Haze Aerosols to Xuzhou, Eastern China: Optical Properties, Sources, Type, and Components, Remote Sens (Basel), 14, 1589, https://doi.org/10.3390/rs14071589, 2022.

Qin, W., Fang, H., Wang, L., Wei, J., Zhang, M., Su, X., Bilal, M., and Liang, X.: MODIS high-resolution MAIAC aerosol
1090   product: Global validation and analysis, Atmos Environ, 264, 118684, https://doi.org/10.1016/j.atmosenv.2021.118684, 2021.

Rahman, M. M., Mahamud, S., and Thurston, G. D.: Recent spatial gradients and time trends in Dhaka, Bangladesh, air pollution and their human health implications, J Air Waste Manage Assoc, 69, 478–501, https://doi.org/10.1080/10962247.2018.1548388, 2019.

Ramachandran, S., Rupakheti, M., Cherian, R., and Lawrence, M. G.: Aerosols heat up the Himalayan climate, Science of The
1095   Total Environment, 164733, https://doi.org/10.1016/j.scitotenv.2023.164733, 2023.

Ramanathan, V. and Carmichael, G.: Global and regional climate changes due to black carbon, Nat Geosci, 1, 221–227, https://doi.org/10.1038/ngeo156, 2008.

Randles, C. A. and Ramaswamy, V.: Direct and semi-direct impacts of absorbing biomass burning aerosol on the climate of southern Africa: a Geophysical Fluid Dynamics Laboratory GCM sensitivity study, Atmos Chem Phys, 10, 9819–9831,
1100   https://doi.org/10.5194/acp-10-9819-2010, 2010.

Randles, C. A., da Silva, A. M., Buchard, V., Colarco, P. R., Darmenov, A., Govindaraju, R., Smirnov, A., Holben, B., Ferrare, R., Hair, J., Shinozuka, Y., and Flynn, C. J.: The MERRA-2 Aerosol Reanalysis, 1980 Onward. Part I: System Description and Data Assimilation Evaluation, J Clim, 30, 6823–6850, https://doi.org/10.1175/JCLI-D-16-0609.1, 2017.

Rasp, S., Pritchard, M. S., and Gentine, P.: Deep learning to represent subgrid processes in climate models, Proceedings of the
1105   National Academy of Sciences, 115, 9684–9689, https://doi.org/10.1073/pnas.1810286115, 2018.

Reichstein, M., Camps-Valls, G., Stevens, B., Jung, M., Denzler, J., Carvalhais, N., and Prabhat: Deep learning and process understanding for data-driven Earth system science, Nature, 566, 195–204, https://doi.org/10.1038/s41586-019-0912-1, 2019.

Ren, Y., Oxford, C. R., Zhang, D., Liu, X., Zhu, H., Dillner, A. M., White, W. H., Chakrabarty, R. K., Hasheminassab, S., Diner, D. J., Le Roy, E. J., Kumar, J., Viteri, V., Song, K., Akoshile, C., Amador-Muñoz, O., Asfaw, A., Chang, R. Y.-W.,
1110   Francis, D., Gahungu, P., Garland, R. M., Grutter, M., Kim, J., Langerman, K., Lee, P.-C., Lestari, P., Mayol-Bracero, O. L., Naidoo, M., Nelli, N., O'Neill, N., Park, S. S., Salam, A., Sarangi, B., Schechner, Y., Schofield, R., Tripathi, S. N., Windwer, E., Wu, M.-T., Zhang, Q., Rudich, Y., Brauer, M., and Martin, R. V.: Black carbon emissions generally underestimated in the global south as revealed by globally distributed measurements, Nat Commun, 16, 7010, https://doi.org/10.1038/s41467-025-62468-5, 2025.

1115   Ricchiazzi, P., Yang, S., Gautier, C., and Sowle, D.: SBDART: A Research and Teaching Software Tool for Plane-Parallel Radiative Transfer in the Earth's Atmosphere, Bull Am Meteorol Soc, 79, 2101–2114, https://doi.org/10.1175/1520-0477(1998)079<2101:SARATS>2.0.CO;2, 1998.

Román, M. O., Schaaf, C. B., Lewis, P., Gao, F., Anderson, G. P., Privette, J. L., Strahler, A. H., Woodcock, C. E., and Barnsley, M.: Assessing the coupling between surface albedo derived from MODIS and the fraction of diffuse skylight over
1120   spatially-characterized landscapes, Remote Sens Environ, 114, 738–760, https://doi.org/10.1016/j.rse.2009.11.014, 2010.

Romshoo, B., Patil, J., Michels, T., Müller, T., Kloft, M., and Pöhlker, M.: Improving the predictions of black carbon (BC) optical properties at various aging stages using a machine-learning-based approach, Atmos Chem Phys, 24, 8821–8846, https://doi.org/10.5194/acp-24-8821-2024, 2024.

Salam, A., Andersson, A., Jeba, F., Haque, Md. I., Hossain Khan, M. D., and Gustafsson, Ö.: Wintertime Air Quality in
1125   Megacity Dhaka, Bangladesh Strongly Affected by Influx of Black Carbon Aerosols from Regional Biomass Burning, Environ Sci Technol, 55, 12243–12249, https://doi.org/10.1021/acs.est.1c03623, 2021.

Saleh, R., Hennigan, C. J., McMeeking, G. R., Chuang, W. K., Robinson, E. S., Coe, H., Donahue, N. M., and Robinson, A. L.: Absorptivity of brown carbon in fresh and photo-chemically aged biomass-burning emissions, Atmos Chem Phys, 13, 7683–7693, https://doi.org/10.5194/acp-13-7683-2013, 2013.

1130 Samset, B. H., Stjern, C. W., Andrews, E., Kahn, R. A., Myhre, G., Schulz, M., and Schuster, G. L.: Aerosol Absorption: Progress Towards Global and Regional Constraints, Curr Clim Change Rep, 4, 65–83, https://doi.org/10.1007/s40641-018-0091-4, 2018a.

Samset, B. H., Sand, M., Smith, C. J., Bauer, S. E., Forster, P. M., Fuglestvedt, J. S., Osprey, S., and Schleussner, C. -F.: Climate Impacts From a Removal of Anthropogenic Aerosol Emissions, Geophys Res Lett, 45, 1020–1029, 1135 https://doi.org/10.1002/2017GL076079, 2018b.

Sayer, A. M., Hsu, N. C., Bettenhausen, C., and Jeong, M. -J.: Validation and uncertainty estimates for MODIS Collection 6 "Deep Blue" aerosol data, Journal of Geophysical Research: Atmospheres, 118, 7864–7872, https://doi.org/10.1002/jgrd.50600, 2013.

Schaaf, C. B., Gao, F., Strahler, A. H., Lucht, W., Li, X., Tsang, T., Strugnell, N. C., Zhang, X., Jin, Y., Muller, J.-P., Lewis, 1140 P., Barnsley, M., Hobson, P., Disney, M., Roberts, G., Dunderdale, M., Doll, C., d'Entremont, R. P., Hu, B., Liang, S., Privette, J. L., and Roy, D.: First operational BRDF, albedo nadir reflectance products from MODIS, Remote Sens Environ, 83, 135–148, https://doi.org/10.1016/S0034-4257(02)00091-3, 2002.

Schuster, G. L.: Inferring black carbon content and specific absorption from Aerosol Robotic Network (AERONET) aerosol retrievals, J Geophys Res, 110, D10S17, https://doi.org/10.1029/2004JD004548, 2005.

1145 Seinfeld, J. H., Kleindienst, T. E., Edney, E. O., and Cohen, J. B.: Aerosol Growth in a Steady-State, Continuous Flow Chamber: Application to Studies of Secondary Aerosol Formation, Aerosol Science and Technology, 37, 728–734, https://doi.org/10.1080/02786820300915, 2003.

Sena, E. T. and Artaxo, P.: A novel methodology for large-scale daily assessment of the direct radiative forcing of smoke aerosols, Atmos Chem Phys, 15, 5471–5483, https://doi.org/10.5194/acp-15-5471-2015, 2015.

1150 Sena, E. T., Artaxo, P., and Correia, A. L.: Spatial variability of the direct radiative forcing of biomass burning aerosols and the effects of land use change in Amazonia, Atmos Chem Phys, 13, 1261–1275, https://doi.org/10.5194/acp-13-1261-2013, 2013.

Soriano Jr, M. A. and Maxwell, R.: Spatial aggregation effects on the performance of machine learning metamodels for predicting transit time to baseflow, Environ Res Commun, 5, 115002, https://doi.org/10.1088/2515-7620/ad0744, 2023.

1155 Subba, T., Gogoi, M. M., Pathak, B., Bhuyan, P. K., and Babu, S. S.: Recent trend in the global distribution of aerosol direct radiative forcing from satellite measurements, Atmospheric Science Letters, 21, https://doi.org/10.1002/asl.975, 2020.

Subba, T., Gogoi, M. M., Moorthy, K. K., Bhuyan, P. K., Pathak, B., Guha, A., Srivastava, M. K., Vyas, B. M., Singh, K., Krishnan, J., Lakshmi Kumar, T. V., and Babu, S. S.: New estimates of aerosol radiative effects over India from surface and satellite observations, Atmos Res, 276, 106254, https://doi.org/10.1016/j.atmosres.2022.106254, 2022.

1160 Sullivan, J. T., Apituley, A., Mettig, N., Kreher, K., Knowland, K. E., Allaart, M., Piters, A., Van Roozendael, M., Veefkind, P., Ziemke, J. R., Kramarova, N., Weber, M., Rozanov, A., Twigg, L., Sumnicht, G., and McGee, T. J.: Tropospheric and stratospheric ozone profiles during the 2019 TROpomi vaLIdation eXperiment (TROLIX-19), Atmos Chem Phys, 22, 11137–11153, https://doi.org/10.5194/acp-22-11137-2022, 2022.

Sun, C., Zhang, Y., Liang, B., Gao, M., Sun, X., Li, F., Ni, X., Sun, Q., Ou, H., Chen, D., Zhou, S., and Zhao, J.: Morphological
1165 and optical properties of carbonaceous aerosol particles from ship emissions and biomass burning during a summer cruise measurement in the South China Sea, Atmos Chem Phys, 24, 3043–3063, https://doi.org/10.5194/acp-24-3043-2024, 2024.

Sundström, A.-M., Arola, A., Kolmonen, P., Xue, Y., de Leeuw, G., and Kulmala, M.: On the use of a satellite remote-sensing-based approach for determining aerosol direct radiative effect over land: a case study over China, Atmos Chem Phys, 15, 505–518, https://doi.org/10.5194/acp-15-505-2015, 2015.

1170 Tian, X., Tang, C., Wu, X., Yang, J., Zhao, F., and Liu, D.: The global spatial-temporal distribution and EOF analysis of AOD based on MODIS data during 2003–2021, Atmos Environ, 302, 119722, https://doi.org/10.1016/j.atmosenv.2023.119722, 2023.

Tiwari, P., Cohen, J. B., Wang, X., Wang, S., and Qin, K.: Radiative forcing bias calculation based on COSMO (Core-Shell Mie model Optimization) and AERONET data, NPJ Clim Atmos Sci, 6, 193, https://doi.org/10.1038/s41612-023-00520-1,
1175 2023.

Tiwari, P., Cohen, J. B., Lu, L., Wang, S., Li, X., Guan, L., Liu, Z., Li, Z., and Qin, K.: Multi-platform observations and constraints reveal overlooked urban sources of black carbon in Xuzhou and Dhaka, Commun Earth Environ, 6, 38, https://doi.org/10.1038/s43247-025-02012-x, 2025.

Wang, D., Liang, S., He, T., Yu, Y., Schaaf, C., and Wang, Z.: Estimating daily mean land surface albedo from MODIS data,
1180 Journal of Geophysical Research: Atmospheres, 120, 4825–4841, https://doi.org/10.1002/2015JD023178, 2015.

Wang, S., Wang, X., Cohen, J. B., and Qin, K.: Inferring Polluted Asian Absorbing Aerosol Properties Using Decadal Scale AERONET Measurements and a MIE Model, Geophys Res Lett, 48, e2021GL094300, https://doi.org/https://doi.org/10.1029/2021GL094300, 2021.

Wei, J., Li, Z., Sun, L., Peng, Y., Liu, L., He, L., Qin, W., and Cribb, M.: MODIS Collection 6.1 3 km resolution aerosol
1185 optical depth product: global evaluation and uncertainty analysis, Atmos Environ, 240, 117768, https://doi.org/10.1016/j.atmosenv.2020.117768, 2020.

Wei, J., Li, Z., Lyapustin, A., Wang, J., Dubovik, O., Schwartz, J., Sun, L., Li, C., Liu, S., and Zhu, T.: First close insight into global daily gapless 1 km PM2.5 pollution, variability, and health impact, Nat Commun, 14, 8349, https://doi.org/10.1038/s41467-023-43862-3, 2023.

1190 Wu, L., Ciren, N., Wang, D., Meng, H., Li, M., Wang, Y., and Chen, T.: Research on simulation and validation methods of aerosol radiative forcing on the Tibetan Plateau based on satellite and ground-based remote sensing observations over the past 20 years, Atmos Res, 107683, https://doi.org/10.1016/j.atmosres.2024.107683, 2024.

Wu, Y., Cheng, T., Liu, D., Allan, J. D., Zheng, L., and Chen, H.: Light Absorption Enhancement of Black Carbon Aerosol Constrained by Particle Morphology, Environ Sci Technol, 52, 6912–6919, https://doi.org/10.1021/acs.est.8b00636, 2018.

1195 Xu, X., Yang, X., Zhu, B., Tang, Z., Wu, H., and Xie, L.: Characteristics of MERRA-2 black carbon variation in east China during 2000–2016, Atmos Environ, 222, 117140, https://doi.org/10.1016/j.atmosenv.2019.117140, 2020.

Yang, S., Liu, Y., Chen, L., Cao, N., Wang, J., and Gao, S.: Direct radiative forcing of light-absorbing carbonaceous aerosol and the influencing factors over China, Atmos Chem Phys, 25, 9335–9355, https://doi.org/10.5194/acp-25-9335-2025, 2025.

Yu, H., Kaufman, Y. J., Chin, M., Feingold, G., Remer, L. A., Anderson, T. L., Balkanski, Y., Bellouin, N., Boucher, O.,

1200 Christopher, S., DeCola, P., Kahn, R., Koch, D., Loeb, N., Reddy, M. S., Schulz, M., Takemura, T., and Zhou, M.: A review of measurement-based assessments of the aerosol direct radiative effect and forcing, Atmos Chem Phys, 6, 613–666, https://doi.org/10.5194/acp-6-613-2006, 2006.

Zaman, S. U., Islam, M. S., Roy, S., Jeba, F., and Salam, A.: Light Absorption Properties of Biomass Burning Emissions in Bangladesh: Current State of Knowledge, in: Vegetation Fires and Pollution in Asia, Springer International Publishing, Cham,

1205 283–298, https://doi.org/10.1007/978-3-031-29916-2_17, 2023.

Zamora, M. L., Peng, J., Hu, M., Guo, S., Marrero-Ortiz, W., Shang, D., Zheng, J., Du, Z., Wu, Z., and Zhang, R.: Wintertime aerosol properties in Beijing, Atmos Chem Phys, 19, 14329–14338, https://doi.org/10.5194/acp-19-14329-2019, 2019.

Zangmeister, C. D., You, R., Lunny, E. M., Jacobson, A. E., Okumura, M., Zachariah, M. R., and Radney, J. G.: Measured in-situ mass absorption spectra for nine forms of highly-absorbing carbonaceous aerosol, Carbon N Y, 136, 85–93,

1210 https://doi.org/10.1016/j.carbon.2018.04.057, 2018.

Zeb, B., Alam, K., Nasir, J., Mansha, M., Ahmad, I., Bibi, S., Malik, S. M., and Ali, M.: Black Carbon aerosol characteristics and radiative forcing over the high altitude glacier region of Himalaya-Karakorum-Hindukush, Atmos Environ, 238, 117711, https://doi.org/10.1016/j.atmosenv.2020.117711, 2020.

Zhou, S. and Cheng, J.: A physics-based atmospheric precipitable water vapor retrieval algorithm by synchronizing MODIS

1215 near-infrared and thermal infrared measurements, Remote Sens Environ, 317, 114523, https://doi.org/10.1016/j.rse.2024.114523, 2025.